JOURNAL OF RESEARCH of the National Bureau of Standards
Vol. 87, No. 2, March–April 1982

Contents

Library of Congress Catalog Card Number: 63-37059

For sale by the Superintendent of Documents, U.S. Government Printing Office
Washington, DC 20402
Single copy price $4.25 Domestic; $5.35 Foreign.
Subscription price: $18.00 a year; $23.50 foreign mailing.
UNITED STATES GOVERNMENT PRINTING OFFICE, WASHINGTON: 1982

JOURNAL OF RESEARCH of the National Bureau of Standards
Vol. 87, No. 2, March–April 1982

Calculation of Aqueous Solubility of Organic Compounds

Yadu B. Tewari, Michele M. Miller, and Stanley P. Wasik

National Bureau of Standards, Washington, DC 20234

August 26, 1981

The aqueous solubility of 14 organic solutes has been calculated from their octanol/water partition coefficient and from their solute activity coefficient in octanol at infinite dilution. The solute activity coefficients were calculated from the Flory-Huggins and Hildebrand-Scatchard (FH-HS) equations and were found to be in good agreement with the activity coefficients determined from GC specific retention volume measurements. The calculated solubilities were in good agreement with the experimental solubilities.

Key words: activity coefficients, gas chromatography, octanol/water partition coefficients, solubility parameters.

1. Introduction

The octanol/water partition coefficient, $K_{o/w}$, and the aqueous solubility, C^s, of organic compounds have been used widely to assess and predict the fate of toxic substances in the marine environment. Both of these quantities have been successfully correlated with environmental partitioning phenomenon such as bioconcentration and sorption. These two quantities are thermodynamically related via eq (1) [1].[1]

$$K_{o/w} = \frac{\gamma_\phi^w}{\gamma_\phi^o} \tag{1}$$

where γ_ϕ^w and γ_ϕ^o are the activity coefficients at infinite dilution based on volume fraction for the solute in water and in *n*-octanol, respectively. The quantity, γ_ϕ^w, is generally defined as the reciprocal of the volume fraction of the solute in water, i.e. $\frac{1}{\phi}$, and is expressed as the reciprocal of the solute concentration in water (C^s) times the molar volume of the solute (V), $1/C^sV$.

Hansch, Quinlan, and Lawrence [2] have developed a method for estimating $K_{o/w}$ based on the additivity principle of thermodynamic properties. On this basis group contributions to log $K_{o/w}$ or Π values are defined by eq (2).

$$\Pi_x = \log K_{o/w}(x) - \log K_{o/w}(h) \tag{2}$$

where $K_{o/w}(x)$ is the partition coefficient of a derivative and $K_{o/w}(h)$ is that of the parent molecule. Despite evidence that Π values are often not additive, usually for steric reasons but sometimes through electronic and hydrogen bonding effects, there are many series of compounds in which Π appears to be invariant.

Equations (1) and (2) suggest that the aqueous solubility, C^s, may be calculated from the molecular structure of the solute provided γ_ϕ^o can be estimated with some degree of accuracy. There are methods [3] available for calculating γ_ϕ^o from the solute physical properties. Because of the simplicity of the calculations, the Flory-Huggins and Hildebrand-Scatchard (FH-HS) method was chosen to evaluate γ_ϕ^o.

According to solution theories [4], the solute activity coefficient (γ_x) based on mole fraction consists of an athermal term and a thermal term. At infinite dilution, in terms of the Flory-Huggins equation for the athermal term and the Hildebrand-Scatchard equation for the thermal term, this may be expressed [5] as

$$ln\gamma_x^\infty = ln\frac{1}{r} + \left(1 - \frac{1}{r}\right) + \frac{V}{RT}(\delta' - \delta)^2 \tag{3}$$

where r is the ratio of the molar volume of the solvent V' to that of the solute V, $\left(\frac{V'}{V}\right)$, and the δ and δ' are, respectively, the solute and solvent solubility parameters. These are defined [6] as

$$\delta = \left(\frac{\Delta E_v}{V}\right)^{1/2} = \left(\frac{\Delta H_v - RT}{V}\right)^{1/2} \tag{4}$$

where ΔE_v and ΔH_v are, respectively, the molar energy and enthalpy of vaporization. At infinite dilution the volume fraction activity coefficient (γ_ϕ^∞) may be expressed in terms of

* Center for Chemical Physics, National Measurement Laboratory.

[1]Figures in brackets indicate literature references at the end of this paper.

mole fraction activity coefficient (γ_X^∞) by the following equation [5, 7].

$$\gamma_\phi^\infty = \gamma_x^\infty \left(\frac{V'}{V}\right) \tag{5}$$

Now combining eq (3) and (5), the solute activity coefficient γ_ϕ^∞ may be expressed as

$$ln\gamma_\phi^\infty = \left(1 - \frac{1}{r}\right) + \frac{V}{RT}(\delta' - \delta)^2 \tag{6}$$

In this paper we are concerned with estimating the solute activity coefficients in water, γ_ϕ^w, using eq 1, from the estimated values of γ_ϕ^o and the experimental values of $K_{o/w}$. Activity coefficients, γ_ϕ^∞, in octanol for a number of solutes have also been calculated from the Flory-Huggins and Hildebrand-Scatchard equations and compared with the experimental values obtained by the gas chromatographic (GC) method.

2. Experimental Procedure

The stationary phase, *n*-octanol, used in this study was obtained from the Aldrich Chemical Company. The purity was checked by GC and was found to be 99 + mole %. The stationary phase was coated onto the support material, Chromosorb W-HP, 100/120 mesh, and the weight percent of coating was determined by an ashing method [8]. A stainless steel column (1/8 in OD) was then packed with a known amount of the coated support and was connected to a Hewlett-Packard 5830A[2] gas chromatograph equipped with a flame ionization detector (FID) for the determination of the solute retention time. The temperature of the column was controlled by circulating water through a copper tubing jacket around the column and by a Haake Model FK temperature regulator which regulated the water temperature to 25.0 ± 0.05 °C.

The column inlet pressure, measured with a precalibrated pressure gauge (range 0–15 PSI), was kept constant during a run by regulating with a precision valve. In order to measure the carrier gas flow rate the column was disconnected from the FID, just before and after the experiment, and a soap bubble flowmeter was connected to the column outlet. The carrier gas was presaturated with *n*-octanol in order to reduce bleeding of the stationary phase.

Since the retention times decreased as the experiment progressed due to column loss of the *n*-octanol, toluene was used as a reference retention time standard and injected with each solute. The measured retention times were then corrected for bleeding using the reference solute retention time.

The solute specific retention volumes (V_g^o) were calculated by using the following equation [9].

$$V_g^o = \frac{t_R \cdot F}{w} \cdot \frac{P_a - P_w}{P_a} \cdot \frac{273.2}{T_a} \cdot \frac{3}{2} \cdot \frac{(P_i/P_a)^2 - 1}{(P_i/P_a)^3 - 1} \tag{7}$$

where t_R is the retention time (min), F is the carrier gas flow rate (ml/min), P_i and P_a are the column inlet and atmospheric pressure (in Torr), P_w is the saturated water vapor pressure (in Torr) at room temperature T_a(°K), and W is the weight (in gram) of stationary phase packed in the column. The reported specific retention volumes listed in column 1 of table 1 are an average of 6 measurements.

3. Results and discussion

The solute activity coefficients at infinite dilution (γ_X^∞) were determined from the following equation [8].

$$ln\gamma_X^\infty = ln\frac{273.2R}{P^oV_g^oM'} - \frac{P^oB}{RT} \tag{8}$$

where M' is the molecular weight of stationary phase, *n*-octanol, (g/mole), P^o and B are, respectively, the vapor pressure (in Torr) and the gas phase second virial coefficient (ml/mole) of the pure solute at temperature T(°K), and R is the gas constant. The second virial coefficients were calculated from the McGlashan and Potter equation [10] using the constants tabulated by Dreisbach [11, 12, 13] and Timmermans [14]. These sources were also used for Antoine constants to calculate values of P^o and for constants for the law of rectilinear diameters to compute values of molar volumes. The solute mole fraction and volume fraction activity coefficients listed in table 1 were calculated using equations 8 and 5. It is estimated that the probable uncertainty in the activity coefficients listed in table 1 is about 2 %.

The solute solubility parameters, δ, listed in table 1 were calculated from their molar enthalpies of vaporization listed in the Dreisbach compilations [11, 12, 13]; whereas the solvent solubility parameter, δ′ was treated as an adjustable parameter. In order to fit the experimental data of the systems studied, two different solubility parameters (δ′) were used, one for aromatic solutes (δ′ = 6.71) and another for aliphatic solutes (δ′ = 9.57). The solute activity coefficients calculated using equation 6 are listed in column 5 of table 1. The agreement between the two sets of data (calculated and experimental activity coefficients) is in general good. The average deviation is 8.7%; however, in a few systems it is as high as 18%. These results suggest that the activity coefficient of a system may be calculated from the knowledge of their

[2] Certain trade names and company products are identified in order to adequately specify the experimental procedure. In no case does such identification imply recommendation or endorsement by the National Bureau of Standards, nor does it imply that the products are necessarily the best available for the purpose.

TABLE 1. *Specific Retention Volumes (V_g^o) and Solute Activity Coefficients in n-Octanol at 25.0 °C.*

Solute	V_g^o (ml/g)	γ_x^∞	γ_ϕ^∞ (expt)	δ^a (cal/cm^3)$^{1/2}$	γ_ϕ^∞ (calc)	$\frac{\gamma_\phi^\infty(\text{expt}) - \gamma_\phi^\infty(\text{calc})}{\gamma_\phi^\infty(\text{expt})} \times 100$
n-Pentane	100.6	2.62	3.59	7.17	4.04	−12.5
n-Hexane	312.5	2.81	3.39	7.33	3.61	−6.5
n-Heptane	943.0	3.06	3.29	7.47	3.21	2.4
n-Octane	2793.	3.36	3.25	7.55	2.99	8.0
1-Hexene	280.5	2.54	3.19	7.38	3.40	6.6
1-Heptene	—	—	—	7.53	3.01	—
1-Octene	2518.	3.00	3.01	7.61	2.79	7.3
1-Nonene	7589.	3.24	2.95	7.73	2.45	16.9
Benzene	669.9	2.07	3.67	9.20	3.94	−7.4
Toluene	2120.	2.18	3.23	8.91	3.32	−2.8
Ethylbenzene	5542.	2.49	3.20	8.79	3.07	4.1
o-Xylene	8317.	2.38	3.12	8.99	3.67	−17.6
m-Xylene	6763.	2.34	3.00	8.82	3.15	−5.0
n-Propylbenzene	13854.	2.76	3.12	8.64	2.71	13.1
Isopropylbenzene	10623.	2.66	3.00	8.61	2.64	12.0

[a] 1 calorie = 4.184 Joules

physical properties using the Flory-Huggins and the Hildebrand-Scatchard equations.

The quantity γ_ϕ^o in eq 1 is defined as the activity coefficient of a solute measured in octanol saturated with water. However, Purnell [15] has shown that γ_ϕ^o for a solute in a binary mixture may be expressed as

$$\frac{1}{\gamma_\phi^o} = \frac{\phi_w}{\gamma_\gamma^{w\prime}} + \frac{\phi_o}{\gamma_\phi^\infty} \qquad (9)$$

where γ_ϕ^∞ and $\gamma_\phi^{w\prime}$ are the solute activity coefficients at infinite dilution in pure octanol and in pure water, respectively, and ϕ_o and ϕ_w are their volume fractions. It has been reported [16] that at equilibrium the volume fraction of water in octanol is 0.0414. The value of γ_ϕ^w for the solutes used in this study vary between 380 and 63,000 while those of γ_ϕ^∞ vary between 3.00 and 3.60. Thus the errors involved in assuming $\gamma_\phi^o = \gamma_\phi^\infty$ and $\gamma_\phi^{w\prime} = \gamma_\phi^w$ are minimal.

The solute activity coefficients in water, γ_ϕ^w, listed in column 3 of table 2, were calculated using the experimental log $K_{o/w}$ and calculated log γ_ϕ^∞ from the Flory-Huggins and Hildebrand-Scatchard equation. Considering that the average standard deviation in the experimental log $K_{o/w}$ is 0.04 and log γ_ϕ^w is 0.03, the agreement between the experimental log γ_ϕ^w (listed in the last column) and the calculated log γ_ϕ^w is very encouraging.

In summary this study suggests that the solute activity coefficient γ_ϕ^∞, may be calculated accurately using the Flory-Huggins and Hildebrand-Scatchard equations, and the solubility of organic compounds in water may be predicted successfully from the knowledge of their octanol/water partition coefficients and the solute activity coefficient calculated from the FH-HS equation.

TABLE 2. *Activity Coefficients and Octanol/Water Partition Coefficients at 25.0 °C.*

Solute	log γ_ϕ^o calculated	log $K_{o/w}$(17) Experimental	log γ_ϕ^w calculated	Experimental (17)
n-Pentane	0.61	3.62	4.23	4.19
n-Hexane	0.56	4.11	4.67	4.73
n-Heptane	0.51	4.66	5.17	5.27
n-Octane	0.48	5.18	5.66	5.80
1-Hexene	0.53	3.39	3.90	3.99
1-Heptene	0.48	3.99	4.47	4.58
1-Octene	0.45	4.57	5.02	5.24
1-Nonene	0.39	5.15	5.54	5.82
Benzene	0.60	2.13[2]	2.73	2.59[2]
Toluene	0.52	2.65	3.17	3.17
Ethylbenzene	0.49	3.13	3.62	3.69
o-Xylene	0.56	3.13	3.69	3.60
m-Xylene	0.50	3.20	3.70	3.73
n-Propylbenzene	0.43	3.69	4.12	4.22
Isopropylbenzene	0.42	3.90	4.32	4.09

We wish to thank Professor Daniel E. Martire, Georgetown University, Washington, D.C., and Dr. Frederick P. Schwarz of this division for helpful discussions of the subject material. We also express our appreciation to the Environmental Protection Agency for financial support.

4. References

[1] Mackay, D.; Bobra, A.; Shiu, W. Y.; Yalkowsky, S. H. Relationships between aqueous solubility and octanol-water partition coefficients. Chemosphere. **2**: 701–711; 1980 December.

[2] Hansch, C.; Quinlan, J. E.; Lawrence, G. L. The linear free-energy relationship between partition coefficients and the aqueous solubility of organic liquids. J. Org. Chem. **33**(1): 347–350; 1968 January.

[3] Prausnitz, J. M.; Anderson, T. F.; Grens, E. A.; Eckert, C. A.; Hsieh, R.; O'Connell, J. P. The Liquid Phase, Chapter 4 in *Computer calculations for multicomponent vapor-liquid and liquid-liquid equilibria*. Englewood Cliffs, N.J.: Prentice-Hall, Inc.; 1980. 39–81.

[4] Ashworth, A. J.; Everett, D. H. The solubility of low-molecular weight hydrocarbons in non-volatile liquids. Faraday Soc. Trans. **56**(11): 1609–1618; 1960 November.

[5] Meen, D. L.; Morris, F.; Purnell, J. H.; Srivastava, A. P. Gas-liquid chromatography measured activity coefficients in non-electrolyte solutions. J. Chem. Soc., Faraday Trans. I. **69**(12): 2080–2086; 1973 December.

[6] Hildebrand, J. H.; Scott, R. L. *Regular solutions*. Englewood Cliffs, N.J.: Prentice-Hall; 1962. 180 p.

[7] Conder, J. R.; Young, C. L. Solution thermodynamics, chapter 5 in *Physico-chemical measurements by gas-liquid chromatography*. New York: John Wiley & Sons; 1979. 154–221.

[8] Tewari, Y. B.; Martire, D. E.; Sheridan, J. P. Gas-liquid partition chromatographic determination and theoretical interpretation of activity coefficients for hydrocarbon solute in alkane solvents. J. Phys. Chem. **74**(11): 2345–2356; 1970 November.

[9] Littlewood, A. B.; Phillips, C. S. G.; Price, D. T. The chromatography of gases and vapours. Part V. Partition analysis with columns of Silicone 702 and of Tritolyl Phosphate. J. Chem. Soc.: 1480–1489; 1955 Part II.

[10] McGlashan, M. L.; Potter, D. J. B. An apparatus for the measurement of the second virial coefficients of vapours; the second virial coefficients of some *n*-alkanes and of some mixtures of *n*-alkanes. Proc. Roy. Soc. A. **267**(1331): 478–500; 1962 June.

[11] Dreisbach, R. R. Physical properties of chemical compounds. A. C. S. Adv. in Chem Ser. **15**; 1955. 536 p.

[12] Dreisbach, R. R. Physical properties of chemical compounds. A. C. S. adv. in Chem. Ser. **22**; 1959. 491 p.

[13] Dreisbach, R. R. Physical properties of chemical compounds. A. C. S. Adv. in Chem. Ser. **29**; 1961. 489 p.

[14] Timmermans, J. *Physico-chemical constants of pure organic compounds*. New York: Elsevier Publishing Co.; 1950. 693 p.

[15] Purnell, J. H.; Vargas de Andrade, J. M. Solution and complexing studies. II. Comparison and correlation of nuclear magnetic resonance and gas-liquid chromatographic data. J. Am. Chem. Soc. **91**(13): 3590–3593; 1974 June 25.

[16] Leo, A.; Hansch, C. Linear Free-Energy Relationships between partitioning Solvent Systems. J. Org. Chem., **36**(11): 1539–1544; 1971 June 4.

[17] Tewari, Y. B.; Miller, M. M.; Wasik, S. P. and Martire, D. E. Aqueous solubility and octanol/water partition coefficients of organic compounds at 25.0 °C. J. Chem. and Eng. Data, (in press).

JOURNAL OF RESEARCH of the National Bureau of Standards
Vol. 87, No. 2, March–April 1982

Enthalpy and Heat-Capacity Standard Reference Material: Synthetic Sapphire (α-Al_2O_3) from 10 to 2250 K

D. A. Ditmars,* S. Ishihara,† S. S. Chang, G. Bernstein,***

National Bureau of Standards, Washington, DC 20234

and

E. D. West

Calorimetrics, Inc., P.O. Box 4146, Boulder, CO 80302

October 14, 1981

Heretofore unpublished enthalpy data which were used in the derivation of smooth enthalpy and heat-capacity data for NBS SRM 720 (α-Al_2O_3, heat capacity and enthalpy standard) are presented along with some details of the high-temperature experiments. Recent NBS low-temperature measurements on SRM 720 are smoothed by a least-squares spline technique and a revised table of certified values for enthalpy and heat capacity of α-Al_2O_3 from 10 K to near the melting point (2250 K) is presented.

Key words: Aluminum oxide; corundum; drop calorimetry; enthalpy; heat capacity; high temperature; Standard Reference Material; synthetic sapphire.

1. Introduction

Standard Reference Material 720 (α-Al_2O_3) has been offered by the NBS Office of Standard Reference Materials since 1970 [1][1] as a heat-capacity and enthalpy standard certified in the temperature range 273.15 K to 2250 K. The relative enthalpy data, whose smoothed representation appears in [1], were obtained in two different types of drop calorimeter: a Bunsen ice calorimeter was used from 273.15 K to 1173.15 K [2] and an adiabatic receiving calorimeter from 1173.15 K to 2250 K. The smoothed relative enthalpy values of [1] rely as well for the absolute ice-point enthalpy ($H_{273.15\ K} - H_{0\ K}$) upon a much earlier low-temperature heat-capacity study [3] on the "Calorimetry Conference Sample" of pure α-Al_2O_3.

A detailed presentation of the original ice-calorimeter enthalpy data along with a description of the smoothing procedure used to obtain the enthalpy and heat-capacity values appearing in [1] has been given in [2]. Unfortunately, the original receiving-calorimeter enthalpy data were never published due to the death of one of the principal experimenters and subsequent personnel changes.

The present work presents this enthalpy data and describes certain aspects of the experiments in the receiving calorimeter. In addition, it documents a re-smoothing of the NBS low-temperature heat-capacity data [4] on SRM 720 obtained since 1970. New smooth heat-capacity data for SRM 720 in the temperature interval 10 K to 2250 K are presented. The present smooth enthalpy data above 273.15 K differ by less than 0.01% from the corresponding values given in [1].

2. High-Temperature Enthalpy Data, 1173 K to 2250 K

Enthalpy data above 1173.15 K were obtained by S. Ishihara in a high-temperature adiabatic receiving calorimeter. Some physical and operational details of this apparatus have been given in [5] and [6]. These experiments were carried out with the calorimeter and furnace containing purified argon gas at about 0.1 atm. pressure. The single-crystal segments of α-Al_2O_3 were contained in a molybdenum capsule (mass: 9.26727 g) with a close-fitting, though not hermetically-sealed, lid. The capsule was suspended from a doubled and twisted loop of 8-mil tungsten wire by a small tantalum hook (hook mass: 0.56097 g). Thirteen evenly-spaced temperatures from 1173 K to 2250 K were chosen, and one day's experiments

* Center for Chemical Physics, National Measurement Laboratory.
† Deceased.
** Center for Materials Science, National Measurement Laboratory.
[1] Figures in brackets indicate literature references at the end of this paper.

TABLE 1. *Heat-Content Data for α-Al_2O_3(s), SRM 720.*

Furnace Temperature T_{68}	Date (1969)	Heat to Calorimeter at 298.15 K	Specimen Mass	$H_T - H_{298.15}$	Deviation from eq. (3) of [2]	
K		J	mol[b]	J mol^{-1}	J mol^{-1}	%
		F 5386.39[a]	0.0295095	99871.6	+ 24.06	+0.024
1173.18	24 Mar.	C 2439.23				
		C 2439.35				
		F 5384.10	0.0295094	99794.3	− 53.24	−0.053
		F 5681.19	0.0303910	103184.8	− 0.57	−0.001
1199.25	7 Apr.	C 2545.30				
		C 2545.25				
		F 5680.87	0.0303914	103174.6	− 10.77	−0.010
		C 2855.86				
1299.16	4 Apr.	F 6474.38	0.0311633	116114.8	+ 41.71	+0.036
		F 6474.87	0.0311633	116156.8	+ 83.71	+0.072
		C 2855.04				
		C 3060.22				
1401.65	10 Mar.	F 6474.38	0.0317601	129563.7	+123.18	+0.095
		F 7175.51	0.0317601	129553.7	+113.38	+0.088
		C 3060.87				
		C 3467.73				
1501.15	19 Mar.	F 7914.37	0.0311937	142549.3	+ 3.60	+0.003
		F 7913.75	0.0311937	142612.1	+ 66.40	+0.047
		C 3565.15				
		F 8441.51	0.0303913	156264.1	− 66.65	−0.043
1604.90	6 Mar.	C 3692.44				
		C 3691.51				
		F 8353.12	0.0298344	156254.7	− 76.05	−0.049
		C 4002.05				
1702.22	4 Mar.	F 9003.15	0.0295487	169249.4	−110.34	−0.065
		F 9003.65	0.0295487	169251.4	−108.34	−0.064
		C 4002.49				
		C 4461.57				
1799.86	27 Mar.	F10147.78	0.0311923	182307.8	−210.67	−0.115
		F10147.78	0.0311923	182307.8	−207.47	−0.114
		F 4461.18				
		F10946.89	0.0311712	196456.3	+ 12.42	+0.006
1902.65	17 Mar.	C 4823.11				
		C 4823.88				
		F10947.56	0.0311671	196479.3	+ 35.42	+0.018
		F11264.44	0.0295326	210507.7	+242.33	+0.115
2004.13	12 Mar.	C 5047.60				
		C 5047.53				
		F11264.44	0.0295218	210509.9	+244.53	+0.116
		C 5125.11				
2101.61	21 Apr.	F11697.26	0.0293640	223816.6	+214.15	+0.096
		F11692.47	0.0293223	223971.5	+369.05	+0.165
		C 5125.11				

TABLE 1. *Continued.*

Furnace Temperature T_{68}	Date (1969)	Heat to Calorimeter at 298.15 K	Specimen Mass	$H_T - H_{298.15}$	Deviation from eq. (3) of [2]	
K		J	mol[b]	J mol^{-1}	J mol^{-1}	%
		C				
2203.28	16 Apr.	F[c]		237748.5	+173.77	+0.073
		F		237625.0	+ 50.27	+0.021
		C				
		F13886.37	0.0315029	244676.5	−322.90	−0.132
2257.11	14 Mar.	C 6178.35				
		C 6177.04				
		F13855.68	0.0313787	244708.7	−290.70	−0.119

[a] "C" prefixes data for empty capsule.
"F" prefixes data for capsule and sample.
[b] Molecular Weight = 101.9613.
[c] Original heat and mass data are available but it was not possible to trace the corrections applied to yield the molar values (col. 5), which were used in evaluation of the smoothing function (eq. (3) of [2]).

consisted of four enthalpy measurements at a single one of these temperatures. The temperature for any particular day was chosen randomly with the aid of a table of random numbers. The first and last enthalpy measurements of a day were made on the same system (either the empty capsule or the same capsule filled with α-Al_2O_3). Experience has shown that this method of scheduling one day's experiments makes it possible to take into account small changes in the pyrometer characteristics or sample capsule mass changes due either to interaction with the sample or with the carbon atmosphere created by the induction furnace susceptor.

Results of the high-temperature measurements are given in table 1. The initial sample capsule temperatures are given in column 1. These were measured with an automatic optical pyrometer which was focused on the bottom of the sample capsule through a small aperture in the furnace susceptor. A separate output signal from the pyrometer was used to control the furnace temperature. Column 3 gives the measured heat to the calorimeter at 298.15 K. The actual terminal temperature of the calorimeter and capsule in the equilibrating period after an experiment was usually less than 320 K. In order to reference all heat data to 298.15 K, it was necessary to add to each measured heat a correction equal to the enthalpy of the capsule (plus sample and carbon contamination, if present) at the terminal temperature of the calorimeter relative to 298.15 K. These corrections ranged from one to two percent of the measured heat. The enthalpy data necessary to calculate the corrections for carbon, tantalum, aluminum oxide, and molybdenum, were taken from references [7], [8], [9] and [2], respectively. The heat content of the aluminum oxide constituted about 55 percent of the total measured heat at all temperatures. The differing values for specimen mass (column 4) indicate that in some experiments different amounts of α-Al_2O_3 were used, though the difference can correspond to at most one or two small pieces of specimen. In the correction of specimen mass data for atmospheric buoyancy, a density of 3.97 g cm^{-3} for α-Al_2O_3 was used. The molar enthalpy values in column 5 were obtained from net heat values (F-C differences from column 3) by division by the applicable specimen mass (column 4).

The present, high-temperature enthalpy results (table 1) and those from [2] in the range 273.15 K to 1173.15 K were represented by a single smoothing function derived by the method of least squares (eq. (3) of [2]). The last two columns of table 1 give the absolute and percent deviation of the present high-temperature data from this equation.

3. Low-Temperature Heat Capacity Data, 8.6 K to 273.15 K

Chang [4] has measured in an automated adiabatic calorimeter [10] the low-temperature heat capacity of α-Al_2O_3 chosen from the same NBS SRM 720 lot as was the material for the high-temperature measurements presented above. A piecewise representation of this low-temperature heat-capacity data, smooth in derivatives to order two, has been obtained using a least-squares spline-fitting technique. The value of this function, as well as its first and second derivatives, match precisely at 273.15 K corresponding values derived from the function [2] representing the enthalpy above 273.15 K.

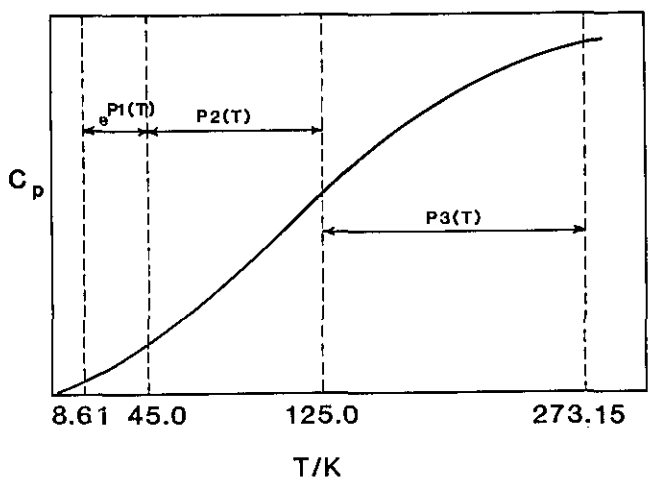

FIGURE 1. Temperature ranges for spline fit of low-temperature heat-capacity data for Al_2O_3.

The piecewise representation is illustrated in figure 1., where P1, P2, and P3 are polynomials of the form

$$\sum_{i=0}^{6} \frac{A_i}{i!} (T - T_0)^i \qquad (1)$$

T_0 is a reference temperature, different for each temperature interval.

45.0 K $> T \geq$ 8.61 K; C_p = exp(P1) J mol^{-1} K^{-1}; T_0 = 8.61 K

$$\begin{aligned} A_0 &= -0.5147E+01 \\ A_1 &= +0.34127E+00 \\ A_2 &= -0.333446E-01 \\ A_3 &= +0.450764E-02 \\ A_4 &= -0.51464E-03 \\ A_5 &= +0.397864E-04 \\ A_6 &= -0.152136E-05 \end{aligned} \qquad (1a)$$

125 K $> T \geq$ 45.0 K; C_p = P2 J mol^{-1} K^{-1}; T_0 = 40.0 K

$$\begin{aligned} A_0 &= +0.6966E+00 \\ A_1 &= +0.59387E-01 \\ A_2 &= +0.40357E-02 \\ A_3 &= +0.95173E-04 \\ A_4 &= -0.35910E-05 \\ A_5 &= -0.6498E-07 \\ A_6 &= +0.4089E-08 \end{aligned} \qquad (1b)$$

273.15 K $> T \geq$ 125 K; C_p = P3 J mol^{-1} K^{-1}; T_0 = 125 K

$$\begin{aligned} A_0 &= +0.21993E+02 \\ A_1 &= +0.38853E+00 \\ A_2 &= +0.13955E-02 \\ A_3 &= -0.83967E-04 \\ A_4 &= +0.19133E-05 \\ A_5 &= -0.31778E-07 \\ A_6 &= +0.29562E-09 \end{aligned} \qquad (1c)$$

The low-temperature heat-capacity data [4] are represented by these smoothing functions with computed percent standard deviations (S_c) for each of the three fitting intervals as follows:

$$\begin{aligned} 45.0 \text{ K} > T \geq 8.61 \text{ K};\ S_c &= 0.97 \\ 125.0 \text{ K} > T \geq 45.0 \text{ K};\ S_c &= 0.13 \\ 273.15 \text{ K} > T \geq 125.0 \text{ K};\ S_c &= 0.05 \end{aligned}$$

According to Chang [4], "It is estimated that the accuracy of the smoothed (low-temperature) values are better than 0.1% at temperatures between 100 and 350 K . . . Below 100 K, the inaccuracy is estimated to become progressively larger, reaching perhaps 1% around 50 K and 10% around 10 K."

4. Enthalpy of SRM 720 (α-Al_2O_3), 10 K to 2250 K

Smooth heat-capacity values were computed from eqs (1), above. Below 8.6 K, a T^3 dependence of heat capacity was assumed. Using these values, the heat-capacity functions were integrated to obtain the absolute enthalpy of α-Al_2O_3 in the temperature range 10 K to 273.15 K. Above 273.15 K, enthalpy and heat-capacity values were derived from the following equation (reproduced for convenience from [2]):

$$H_T - H_{273.15} = AT^{-2} + BT^{-1} + C\ln T + K + DT + ET^2 + FT^3 + GT^4 + HT^5 \text{ J mol}^{-1} \qquad (2)$$

$$\begin{aligned} A &= +6.6253E+07 & E &= -8.57516E-02 \\ B &= -4.54238E+06 & F &= +4.299063E-05 \\ C &= -5.475599E+04 & G &= -1.15192E-08 \\ K &= +2.5819702E+05 & H &= +1.26351E-12 \\ D &= +2.574076E+02 \end{aligned}$$

Table 2 presents these smooth heat-capacity and enthalpy data for α-Al_2O_3.

TABLE 2. *Enthalpy and heat capacity of standard reference material 720.*

Temp	H_T-H_{0K}	C_p	Temp.	H_T-H_{0K}	C_p
K	J mol^{-1}[b]	J mol^{-1} K^{-1}	K	J mol^{-1}	J mol^{-1} K^{-1}
			440	2295_3	100.6_9
10	0.02_3	0.009_1	450	2396_5	101.7_1
15	0.11_5	0.030_7	460	2498_7	102.6_8
20	0.36_4	0.073_2	470	2601_8	103.6_0
25	0.89_8	0.14_6	480	2705_9	104.4_8
30	1.90_5	0.26_5	490	2810_8	105.3_3
35	3.64_6	0.44_3	500	2916_5	106.1_3
40	6.46_0	0.69_7	510	3023_0	106.9_0
45	10.7_7	1.04_6	520	3130_3	107.6_4
50	17.1_1	1.50_6	530	3238_3	108.3_5
60	38.1_8	2.79_3	540	3347_0	109.0_2
70	74.6_8	4.59_2	550	3456_3	109.6_7
80	$131._7$	6.90_1	560	3566_3	110.2_9
90	$214._2$	9.67_3	570	3676_9	110.8_9
100	$326._6$	12.85_5	580	3788_1	111.4_6
110	$472._4$	16.34_7	590	3899_8	112.0_2
120	$654._3$	20.0_7	600	4012_1	112.5_5
130	$874._3$	23.9_5	610	4124_9	113.0_6
140	$1133._7$	27.9_3	620	4238_2	113.5_5
150	$1433._1$	31.9_5	630	4352_0	114.0_2
160	$1772._7$	35.9_5	640	4466_3	114.4_8
170	$2152._0$	39.9_0	650	4581_0	114.9_2
180	$2570._3$	43.7_5	660	4696_1	115.3_5
190	$3026._7$	47.5_0	670	4811_7	115.7_6
200	$3519._9$	51.1_2	680	4927_6	116.1_6
210	$4048._7$	54.6_1	690	5044_0	116.5_5
220	$4611._6$	57.9_5	700	5160_7	116.9_2
230	$5207._1$	61.1_4	720	5395_3	117.6_4
240	$5833._9$	64.1_8	740	5631_3	118.3_2
250	$6490._3$	67.0_8	760	5868_5	118.9_6
260	$7175._0$	69.8_2	780	6107_1	119.5_6
270	$7886._3$	72.4_2	800	6346_8	120.1_4
273.15	$8115._6$	73.2_1	820	6587_6	120.6_9
280	$8622._8$	74.8_7	840	6829_5	121.2_1
290	$9383._2$	77.2_0	860	7072_4	121.7_1
298.15	1002_0	79.0_1	880	7316_3	122.2_0
300	1016_6	79.4_1	900	7561_2	122.6_6
310	1097_1	81.5_1	920	7807_0	123.1_1
320	1179_6	83.4_9	940	8053_6	123.5_5
330	1264_1	85.3_7	960	8301_1	123.9_7
340	1350_3	87.1_6	980	8549_5	124.3_7
350	1438_3	88.8_4	1000	8798_6	124.7_7
360	1528_0	90.4_5	1020	9048_6	125.1_6
370	1619_2	91.9_7	1040	9299_2	125.5_3
380	1711_9	93.4_1	1060	9550_7	125.9_0
390	1806_0	94.7_8	1080	9802_8	126.2_6
400	1901_4	96.0_8	1100	1005_{60}	126.6_1
410	1998_2	97.3_2	1120	1030_{90}	126.9_5
420	2096_1	98.5_0	1140	1056_{40}	127.2_9
430	2195_1	99.6_2	1160	1081_{80}	127.6_1

TABLE 2. *Continued*

Temp	H_T-H_{0K}	C_p	Temp	H_T-H_{0K}	C_p
K	J mol^{-1}	J mol^{-1} K^{-1}	K	J mol^{-1}	J mol^{-1} K^{-1}
1180	1107_{40}	127.9_4	1700	1790_{80}	$134._{31}$
1200	1133_{00}	$128._{25}$	1750	1858_{10}	$134._{73}$
1250	1197_{30}	$129._{01}$	1800	1925_{50}	$135._{13}$
1300	1262_{00}	$129._{74}$	1850	1993_{20}	$135._{50}$
1350	1327_{10}	$130._{43}$	1900	2061_{00}	$135._{83}$
1400	1392_{40}	$131._{08}$	1950	2129_{00}	$136._{18}$
1450	1458_{10}	$131._{70}$	2000	2197_{20}	$136._{50}$
1500	1524_{10}	$132._{29}$	2050	2265_{50}	$136._{80}$
1550	1590_{40}	$132._{84}$	2100	2334_{00}	$137._{10}$
1600	1657_{00}	$133._{36}$	2150	2402_{60}	$137._{41}$
1650	1723_{80}	$133._{85}$	2200	2471_{40}	$137._{73}$
			2250	2540_{30}	$138._{06}$

[a] Temperatures expressed on IPTS-68 scale.

[b] Molecular Weight = 101.9613.

5. References

[1] NBS Certificate, Standard Reference Material 720, Synthetic Sapphire (Al_2O_3); August 26, 1970.

[2] Ditmars, D. A.; Douglas, T. B., J. Res. Nat. Bur. Stand. (U.S.), **75A** (Phys. and Chem.), No. 5, 401 (Sept-Oct 1971).

[3] Furukawa, G. T.; Douglas, T. B.; McCoskey, R. E.; Ginnings, D. C., J. Res. Nat. Bur. Stand. (U.S.), **57**, No. 2, 67 (1956) RP2694.

[4] Chang, S. S., Proceedings of the Seventh Symposium on Thermophysical Properties, ASME; NBS, Gaithersburg, MD., May 10-12, 1977, 83 (1977).

[5] West, E. D.; Ishihara, S., A calorimetric determination of the enthalpy of graphite from 1200 to 2600 K in *Advances in Thermophysical Properties at Extreme Temperatures and Pressures*, p. 146, ASME, New York, (1965). See also NBS Special Publication No. 300. vol. **6**, p. 220 (1970).

[6] Ditmars, D. A.; Cezairliyan, A.; Ishihara, S.; Douglas, T. B.; NBS Special Publication 260-55 (1977).

[7] Kelley, K. K., "Contributions to the data on theoretical metallurgy, XIII. High-temperature heat-content, heat-capacity, and entropy data for the elements and inorganic compounds," U.S. Bureau of Mines Bulletin. *584*, (1960).

[8] Sterrett, K. F.; Wallace, W. E., J. Am. Chem. Soc. **80**, 3176 (1958).

[9] Reilly, M. L.; Furukawa, G. T., Critical analysis of the heat-capacity data of the literature and evaluation of thermodynamic properties of Cr, Mo, and W from 0 to 300 K, NSRDS-NBS (to be published).

[10] Chang, S. S., Proceedings of the Seventh Symposium on Thermophysical Properties, ASME; NBS, Gaithersburg, MD., May 10-12, 1977, 75 (1977).

JOURNAL OF RESEARCH of the National Bureau of Standards
Vol. 87, No. 2, March–April 1982

Buoyant Convection Computed in a Vorticity, Stream-Function Formulation

Ronald G. Rehm,* Howard R. Baum,† and P. Darcy Barnett*

National Bureau of Standards, Washington, DC 20234

September 2, 1981

Model equations describing large scale buoyant convection in an enclosure are formulated with the vorticity and stream function as dependent variables. The mathematical model, based on earlier work of the authors, is unique in two respects. First, it neglects viscous and thermal conductivity effects. Second the fluid is taken to be thermally expandable: large density variations are allowed while acoustic waves are filtered out. A volumetric heat source of specified spatial and temporal variation drives the flow in a two-dimensional rectangular enclosure. An algorithm for solution of the equations in this vorticity, stream-function formulation is presented. Results of computations using this algorithm are presented. Comparison of these results with those obtained earlier by the authors using a finite difference code to integrate the primitive equations show excellent agreement. A method for periodically smoothing the computational results during a calculation, using Lanczos smoothing, is also presented. Computations with smoothing at different time intervals are presented and discussed.

Key words: buoyant convection; finite difference computations; fire-enclosure; fluid flow; Lanczos smoothing; partial differential equations; stream function; vorticity.

1. Introduction

Over the past few years, the National Bureau of Standards has sponsored a joint research project between the Center for Fire Research and the Center for Applied Mathematics to develop, starting from basic conservation laws, a mathematical model of fire development within a room. Large scale convection is an essential component of such a model because this fluid motion governs the smoke and hot gas transport within a room and also supplies fresh oxygen to the fuel to sustain combustion. Therefore, development of a mathematical model of buoyant convection was begun as a first step toward a more complete room-fire model, which would include effects of combustion chemistry, radiation, and smoke dynamics. The mathematical model for convection, the partial differential equations, and boundary conditions, are derived in reference [1].[1]

As noted in earlier papers [1,2] the mathematical model is unique in two respects. First, it is assumed that viscous and thermal conductivity effects are negligible. Second, the fluid has been taken to be thermally expandable so that large temperature and density variations can be taken into account, while acoustic waves have been filtered out to reduce computational time.

The model equations were integrated for density, pressure, and velocity components by finite difference techniques; the algorithm is presented in detail in reference [2]. The algorithm has been verified by comparison with solutions to the equations in special cases obtained by analytical and independent numerical means; the verification is described in references [3] and [4] and in the present study.

In section 2 the model equations are recast into a form such that the dependent variables are density, pressure, vorticity, velocity potential, and stream function. This formulation, the so-called vorticity, stream-function formulation, is an alternate one to that described in reference [2], which we call a primitive-variables formulation. An algorithm for integration of the equations in a vorticity, stream-function formulation is also presented in this section.

* Center for Applied Mathematics, National Engineering Laboratory.
† Center for Fire Research, National Engineering Laboratory.

Results from the two algorithms are compared: the results are in such good agreement that the difference cannot be seen on plots of the dependent variables. This comparison represents a final check on the validity of the integration algorithms and their computer code implementations. Therefore, we believe that the solutions obtained by these computations are excellent approximate solutions to the model partial differential equations presented in reference [1].

The model has been developed for two-dimensional, time-dependent fires evolving in a room (rectangular enclosure). The fire has been modeled as a volumetric heat source of specified spatial extent and temporal behavior. In section 3 density or temperature (which are inversely related at any specified time in this model), vorticity, pressure, and velocity potential plots at fixed times during the heating are shown for a sample computation.

It is well known that, because of the quadratic nonlinearity in convection, initially smooth flow fields become increasingly more furrowed as time progresses; i.e., energy cascades from lower wavenumber modes to higher ones. The computational results display this behavior, and the flow field becomes more intricate with increasing time, the resolution of the grid providing the only limitation to the resolvable detail. However, such an accumulation of energy at a wavenumber inversely proportional to the grid size is both unphysical, and, if the computation is carried out long enough, disastrous. Local gradients of the dependent variables become much too large and the computation ultimately fails. Therefore, also shown in section 3 of this paper are preliminary considerations of smoothing or filtering of the computational results. Such smoothing acts analogously to viscosity and can be used to prolong the lifetime of the computation. A brief discussion of the effects of a particular type (Lanczos) of smoothing is presented, and results obtained using this smoothing are shown.

2. Formulation

2.1. Continuous equations

In an earlier paper [1], the authors had derived a set of nonlinear equations describing very nonadiabatic buoyant flows of a nondissipative perfect gas. The magnitude and the spatial variation of the heat source (representing the exothermic reaction in a fire) were taken as known. The fluid and the fire source were assumed confined in a closed rectangular room with the center of the source along the floor. In contrast to reference [1], in this paper we consider only a completely enclosed room (no leaks), and when difference equations are introduced, we confine attention to the two dimensional evolution of the flow.

In this section, the equations derived in reference [1] for a two-dimensional configuration are rewritten so that vorticity and the stream function are primary variables, and the finite difference methods used to solve the revised equations are presented.

Equations (11) of reference [1] are

$$\begin{aligned}
&\frac{\partial \rho}{\partial t} + \frac{\partial}{\partial x_i}(\rho u_i) = 0 \\
&\rho\left(\frac{\partial u_i}{\partial t} + u_j \frac{\partial u_i}{\partial x_j}\right) + \frac{\partial (p - p_o(t))}{\partial x_i} - \rho k_i g = 0 \\
&\rho C_p\left(\frac{\partial T}{\partial t} + u_j \frac{\partial T}{\partial x_j}\right) - \frac{dp_o}{dt} = Q(x_i,t) \\
&p_o(t) = \rho R T
\end{aligned} \tag{1}$$

Here ρ is density, u_i the velocity in the i^{th} coordinate direction ($i = 1, 2, 3$), p is the pressure excess above the mean pressure $p_o(t)$ in the room, T the temperature, C_p the constant-pressure specific heat, R the gas constant, $k_i g$ is the gravitational acceleration, and $Q(x_i,t)$ the specified volumetric heat source. The spatially uniform mean pressure $p_o(t)$ depends only upon time and increases because of the heating within the room. It is determined in a completely enclosed room by the equation

$$\frac{dp_o}{dt} = \frac{\gamma-1}{V}\int_V Q(x_i,t)dV \tag{2}$$

where γ is the ratio of specific heats, V is the volume of the room and the integration is performed over this entire volume.

We take the substantial derivative of the equation of state and use this with the energy equation to eliminate the temperature. The resulting equation describes the evolution of the density under heating

$$\frac{\partial \rho}{\partial t} + u_i \frac{\partial \rho}{\partial x_i} = -\rho \frac{\partial u_i}{\partial x_i} = -\rho D(x_j,t) \tag{3}$$

where

$$D(x_j,t) = \frac{1}{\gamma p_o(t)}\left[(\gamma-1)Q(x_j,t) - \frac{dp_o}{dt}\right]. \tag{4}$$

Equation (3) and the continuity equation identify $D(x_i,t)$ as the divergence

$$\frac{\partial u_i}{\partial x_i} = D(x_j,t)\ . \tag{5}$$

Finally, as in reference [1], the equation for the spatially variable portion of the pressure is obtained by dividing the momentum equations by density and taking the divergence of these equations. The resulting equation is

$$\frac{\partial}{\partial x_i}\left(\frac{1}{\rho}\frac{\partial p}{\partial x_i}\right) = -\left[\frac{\partial}{\partial x_i}\left(u_j\frac{\partial u_i}{\partial x_j}\right) + \frac{\partial D(x_j,t)}{\partial t}\right] \tag{6}$$

The boundary conditions on these equations are that velocity normal to any (impermeable) wall vanish.

$$u_i n_i = 0 \tag{7}$$

where n_i are the normal components of a vector describing the boundary wall. From eqs (1) and these conditions, the appropriate boundary conditions on the pressure equation are obtained

$$n_i \frac{\partial p}{\partial x_i} = \rho g\, n_i k_i \tag{8}$$

In two dimensions (no dependence on z), these equations become

$$\begin{aligned}
&\frac{\partial \rho}{\partial t} + u\frac{\partial \rho}{\partial x} + v\frac{\partial \rho}{\partial y} = -\rho D(x,y,t)\\
&\frac{\partial u}{\partial t} + 1/2\,\frac{\partial}{\partial x}(u^2+v^2) - v\omega = -\frac{1}{\rho}\frac{\partial p}{\partial x}\\
&\frac{\partial v}{\partial t} + 1/2\,\frac{\partial}{\partial y}(u^2+v^2) + u\omega = -\frac{1}{\rho}\frac{\partial p}{\partial y} - g\\
&\frac{\partial}{\partial x}\left(\frac{1}{\rho}\frac{\partial p}{\partial x}\right) + \frac{\partial}{\partial y}\left(\frac{1}{\rho}\frac{\partial p}{\partial y}\right) = -\frac{\partial D}{\partial t} + \frac{\partial}{\partial x}(v\omega) - \frac{\partial}{\partial y}(u\omega) - 1/2\,\nabla^2(u^2+v^2)
\end{aligned} \tag{9}$$

where x and y are the horizontal and vertical coordinates with velocity components u and v respectively and

$$\omega = \frac{\partial v}{\partial x} - \frac{\partial u}{\partial y} \tag{10}$$

is the only nonzero component of vorticity.

Equations (9) can be recast into a form in which the vorticity, the stream function and the velocity potential, together with density and pressure, are primary dependent variables. The velocity components can be written as

$$\begin{aligned} u &= \frac{\partial \phi}{\partial x} + \frac{\partial \psi}{\partial y} \\ v &= \frac{\partial \phi}{\partial y} - \frac{\partial \psi}{\partial x} \end{aligned} \tag{11}$$

where ϕ is the velocity potential and ψ the stream function. Equations for ϕ and ψ come from the divergence eq (5) and from the definition for vorticity (10)

$$\nabla^2 \phi = D(x,y,t) \tag{12a}$$

$$\nabla^2 \psi = -\omega \tag{12b}$$

For these two elliptic equations, the stream function and the normal derivative of the potential are zero on the boundary:

$$\frac{\partial \phi}{\partial n} = 0 \quad \text{and} \quad \psi = 0 \tag{13}$$

The equation describing the density evolution remains as it was in eqs (9), and an equation for the vorticity evolution comes from taking the curl of the two velocity equations in eqs (9).

$$\frac{\partial \omega}{\partial t} + u\frac{\partial \omega}{\partial x} + v\frac{\partial \omega}{\partial y} + \omega D = -\frac{\partial}{\partial x}\left(\frac{1}{\rho}\frac{\partial p}{\partial y}\right) + \frac{\partial}{\partial y}\left(\frac{1}{\rho}\frac{\partial p}{\partial x}\right) \tag{14}$$

In figure 1 a schematic diagram of a fire evolving in a room in two dimensions and a set of coordinate axes are shown. It is assumed that initially the enclosure is filled with quiescent, stratified fluid of density $\rho_o(y)$.

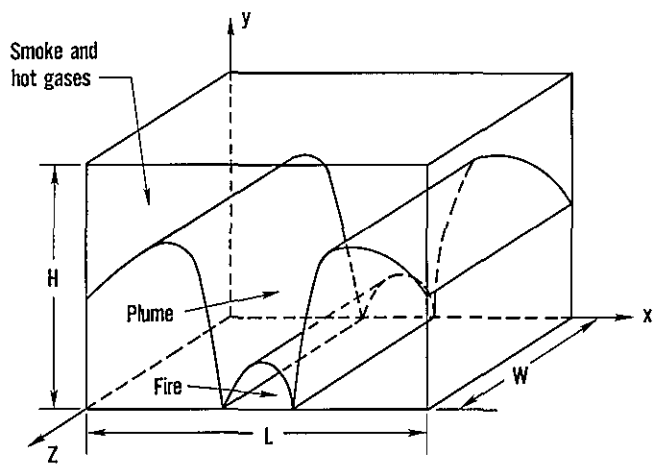

FIGURE 1. Schematic diagram of a two dimensional fire evolving in a room: it is assumed that there is no dependence upon z of any of the properties of the fire or of the induced flow field. The fire, localized along the floor, has a plume of combustion products rising above it. The smoke and hot gases rise to the ceiling and fill the room from the top down.

We define a density difference from ambient and a pressure difference as follows

$$\tilde{\rho}(x,y,t) = \rho(x,y,t) - \rho_o(y)$$
$$\tilde{p}(x,y,t) = p(x,y,t) - p_o(t) + g\int_o^y \rho_o(y')\,dy'$$

These differences $\tilde{\rho}$ and $\tilde{p}$ need not be small compared with $\rho_o(y)$ and $p_o(t)$ respectively. Then the first and last of eqs (9) and eq (14) become

$$\begin{aligned}
\frac{\partial\tilde{\rho}}{\partial t} + u\frac{\partial\tilde{\rho}}{\partial x} + v\frac{\partial\tilde{\rho}}{\partial y} + v\frac{d\rho_o}{dy} &= -(\rho_o(y) + \tilde{\rho})D(x,y,t) \\
\frac{\partial\omega}{\partial t} + u\frac{\partial\omega}{\partial x} + v\frac{\partial\omega}{\partial y} + \omega D &= -\frac{\partial}{\partial x}\left[(1/(\rho_o+\tilde{\rho}))\left(\frac{\partial\tilde{p}}{\partial y} + g\tilde{\rho}\right)\right] \\
&\quad + \frac{\partial}{\partial y}\left[(1/(\rho_o + \tilde{\rho}))\frac{\partial\tilde{p}}{\partial x}\right] \qquad (15) \\
\frac{\partial}{\partial x}\left[(1/(\rho_o + \tilde{\rho}))\frac{\partial\tilde{p}}{\partial x}\right] + \frac{\partial}{\partial y}\left[(1/(\rho_o + \tilde{\rho}))\frac{\partial\tilde{p}}{\partial y}\right] &= -\frac{\partial}{\partial y}[g\tilde{\rho}/(\rho_o + \tilde{\rho})] \\
&\quad - \frac{\partial D}{\partial t} - (1/2)\nabla^2(u^2+v^2) \\
&\quad + \frac{\partial}{\partial x}(v\omega) - \frac{\partial}{\partial y}(u\omega)
\end{aligned}$$

Equations (11), (12) and (15) constitute the complete set of differential equations for numerical integration in the vorticity, stream function formulation. The boundary conditions are given by eqs (8), with $\tilde{p}$ and $\tilde{\rho}$ replacing p and ρ, and by eqs (13).

Finally, we form dimensionless equations using the density $\rho_{oo} \equiv \rho_o(0)$, the height of the room H as the length scale and the free fall time $(H/g)^{1/2}$ as the time scale. Then, denoting dimensionless quantities with a hat

$$\begin{aligned}
&\hat{\rho} = \tilde{\rho}/\rho_{oo}, \quad \hat{p} = \tilde{p}/(\rho_{oo}gH), \quad \hat{\rho}_o = \rho_o/\rho_{oo} \\
&\hat{\phi} = \frac{1}{H\sqrt{gH}}\phi, \quad \hat{\psi} = \frac{1}{H\sqrt{gH}}\psi, \quad \omega = \sqrt{\frac{H}{g}}\omega \qquad (16) \\
&\hat{u} = \frac{u}{\sqrt{gH}}, \quad \hat{v} = \frac{v}{\sqrt{gH}}, \quad \hat{x} = \frac{x}{H}, \quad \hat{y} = \frac{y}{H} \\
&t = t/\sqrt{(H/g)}
\end{aligned}$$

Equations (11), (12) and (15) remain exactly the same in dimensionless form with g set equal to one. Subsequently, in this paper all quantities will be understood to be dimensionless, and the hat notation will be dropped. For the dimensionless coordinates, we note that $0 \leqslant x \leqslant 1/AR$ and $0 \leqslant y \leqslant 1$ where $AR \equiv H/L$.

2.2. Discrete Equations

2.2.1. The Basic Algorithm

In this section the finite difference equations and the boundary relations for the solution algorithm are presented. In figure 2a, the two-dimensional rectangular enclosure in dimensionless variables is shown together with a schematic representation of the spatial grids used for the finite difference scheme. The grid formed

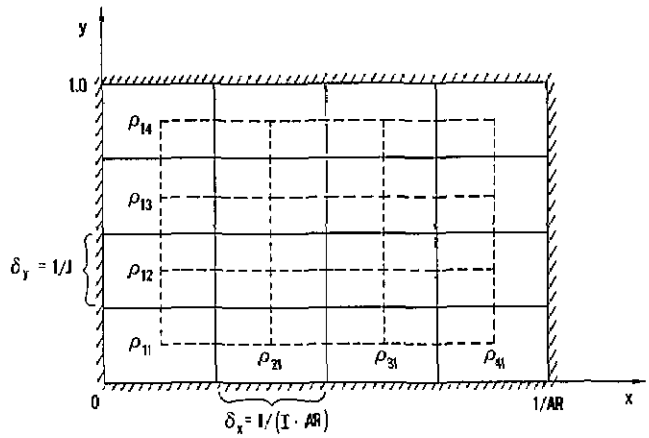

FIGURE 2a. Rectangular enclosure in dimensionless variables $0 \leq x \leq \frac{1}{AR}$, $0 \leq y \leq 1$. The mesh upon which the difference scheme is based is shown schematically for ($I = J = 4$) as a grid of solid lines. The mesh of dashed lines joins the center points of the basic mesh cells and is the grid upon which the pressure computation is performed.

from solid lines represents the basic mesh into which the enclosure is divided: in general there are I mesh cells in the x-direction and J mesh cells in the y-direction.

Upon this basic mesh, the two components of the vector (u,v) and single component of the vector vorticity $\omega = \frac{\partial v}{\partial x} - \frac{\partial u}{\partial y}$ are defined.

The second grid, formed by joining the center points of the basic grid cells and denoted by dashed lines, is that upon which scalar quantities such as density ρ and pressure p are defined. In figure 2a the densities in the left-hand column of cells and in the bottom row of cells are shown to indicate how they are enumerated for the numerical computation.

In figure 2b a typical mesh cell is shown, illustrating where all of the dependent variables in the finite difference scheme are defined relative to the cell.

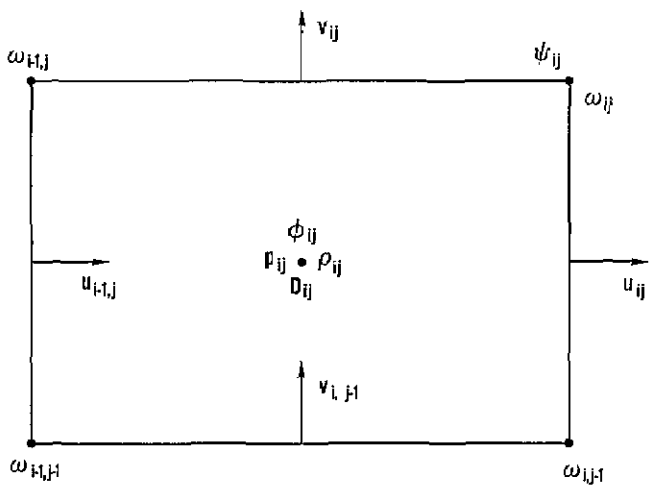

FIGURE 2b. A typical mesh cell, with center located at $x = (i - 1/2)\,\delta x$ and $y = (j - 1/2)\,\delta y$, illustrating where all dependent variables for the finite difference scheme are defined.

The following discretely evaluated functions will denote approximations to the corresponding solutions to eqs (11), (12) and (15):

$$\begin{aligned}
\phi_{ij}^n &\cong \phi((i-1/2)\delta x,(j-1/2)\delta y,n\delta t)\\
\psi_{ij}^n &\cong \psi(i\delta x,j\delta y,n\delta t)\\
u_{ij}^n &\cong u(i\delta x,(j-1/2)\delta y,n\delta t)\\
v_{ij}^n &\cong ((i-1/2)\delta x,j\delta y,n\delta t)\\
\rho_{ij}^n &\cong \rho((i-1/2)\delta x,(j-1/2)\delta y,n\delta t)\\
p_{ij}^n &\cong p((i-1/2)\delta x,(j-1/2)\delta y,n\delta t)\\
D_{ij}^n &= D((i-1/2)\delta x,(j-1/2)\delta y,n\delta t)\ ,\\
\omega_{ij}^n &\cong \omega(i\delta x,j\delta y,n\delta t)
\end{aligned} \tag{17}$$

where $\delta x = 1/(I\cdot AR)$ and $\delta y = 1/J$ are the mesh cell sizes in the x- and y-directions respectively and where δt is the time-step size. Such a staggered grid is commonly used for multidimensional finite difference integrations [5].

With this notation, the following set of finite difference equations was used to approximate eqs (11), (12) and (15) and boundary conditions (8) and (13):

For the first of eqs (15), $1 \leqslant i \leqslant I$, $1 \leqslant j \leqslant J$ and $n \geqslant 2$,

$$\begin{aligned}
\tilde{\rho}_{ij}^{n+1} = \frac{1}{1+(1/2)D_{ij}^n\delta t}\{&\tilde{\rho}_{ij}^{n-1}(1-(1/2)D_{ij}^n\delta t) - 2\delta t(F_{\rho x_{ij}}^n + F_{\rho y_{ij}}^n\\
&+ (1/2)D_{ij}^n\rho_o(j))\}
\end{aligned} \tag{18}$$

where

$$\begin{aligned}
\tilde{\rho}_{ij}^n &= \rho_{ij}^n - \rho_o(j) = \text{the density difference from the initial density,}\\
\rho_o(j) &= \exp[-(j-1/2)\delta y/Y_s] = \text{the ambient, initial stratification,}\\
Y_s &= \text{the stratification length scale.}
\end{aligned} \tag{19}$$

The flux terms $F_{\rho x_{ij}}^n$ and $F_{\rho y_{ij}}^n$ for $1 \leqslant i \leqslant I$, $1 \leqslant j \leqslant J$ are given by

$$F_{\rho x_{ij}}^n = \left(\frac{2\rho_o(j) + \tilde{\rho}_{i+1,j}^n + \tilde{\rho}_{i-1,j}^n}{4}\right)\left(\frac{u_{ij}^n - u_{i-1,j}^n}{\delta x}\right) + \left(\frac{\tilde{\rho}_{i+1,j}^n - \tilde{\rho}_{i-1,j}^n}{2\delta x}\right)\left(\frac{u_{ij}^n + u_{i-1,j}^n}{2}\right) \tag{20a}$$

$$\begin{aligned}
F_{\rho y_{ij}}^n = &\frac{\rho_o(j+1) + \rho_o(j-1) + \tilde{\rho}_{i,j+1}^n + \tilde{\rho}_{i,j-1}^n}{4}\left(\frac{v_{ij}^n - v_{i,j-1}^n}{\delta y}\right)\\
&+ \frac{\rho_o(j+1) - \rho_o(j-1) + \tilde{\rho}_{i,j+1}^n - \tilde{\rho}_{i,j-1}^n}{2\delta y}\left(\frac{v_{ij}^n + v_{i,j-1}^n}{2}\right)
\end{aligned} \tag{20b}$$

For the second of eqs (15), $1 \leqslant i \leqslant I$, $1 \leqslant j \leqslant J$ and $n \geqslant 2$,

$$\omega_{ij}^{n+1} = \omega_{ij}^{n-1} - 2\delta t \left\{ \frac{1}{2\delta x} \left(u_{\omega i+1,j}^{n} \omega_{i+1,j}^{n} - u_{\omega i-1,j}^{n} \omega_{i-1,j}^{n} \right) + \frac{1}{2\delta y} \left(v_{\omega i,j+1}^{n} \omega_{i,j+1}^{n} - v_{\omega i,j-1}^{n} \omega_{i,j-1}^{n} \right) + G_{ij}^{n} \right\} \tag{21}$$

where

$$\begin{aligned} v_{\omega ij}^{n} &= (1/2)(v_{ij}^{n} + v_{i+1,j}^{n}) , \\ u_{\omega ij}^{n} &= (1/2)(u_{i,j+1}^{n} + u_{ij}^{n}) , \end{aligned} \tag{22}$$

$$\begin{aligned} G_{ij}^{n} = \frac{2}{\delta x \delta y} \Bigg[& \frac{\tilde{p}_{i+1,j+1}^{n} - \tilde{p}_{i+1,j}^{n} + (\tilde{\rho}_{i+1,j+1}^{n} + \tilde{\rho}_{i+1,j}^{n})(\delta y/2)}{\rho_o(j+1) + \rho_o(j) + \tilde{\rho}_{i+1,j+1}^{n} + \tilde{\rho}_{i+1,j}^{n}} \\ & - \frac{\tilde{p}_{i,j+1}^{n} - \tilde{p}_{ij}^{n} + (\tilde{\rho}_{i,j+1}^{n} - \tilde{\rho}_{ij}^{n})(\delta y/2)}{\rho_o(j+1) + \rho_o(j) + \tilde{\rho}_{i,j+1}^{n} + \tilde{\rho}_{i,j}^{n}} \\ & - \frac{\tilde{p}_{i+1,j+1}^{n} - \tilde{p}_{i,j+1}^{n}}{2\rho_o(j+1) + \tilde{\rho}_{i+1,j+1}^{n} + \tilde{\rho}_{i,j+1}^{n}} + \frac{\tilde{p}_{i+1,j}^{n} - \tilde{p}_{ij}^{n}}{2\rho_o(j) + \tilde{\rho}_{i+1,j}^{n} + \tilde{\rho}_{ij}^{n}} \Bigg] \end{aligned} \tag{23}$$

Equation (18) employs a second-order accurate temporal discretization which eliminates instability that would arise if leap frog had been applied. The first of eqs (15) has an undifferentiated term $\tilde{\rho}D(x,y,t)$ that is well known to lead to a computational instability for ordinary differential equations when leap frog is used. Reference [10] discusses the simple change in temporal differencing used here to eliminate this instability.

Equation (21) uses a straightforward leapfrog temporal differencing, and both eqs (18) and (21) are started by using the same spatial discretization and an explicit, first-order time step.

At each time step, after the vorticity has been updated, three elliptic equations must be solved, eqs (12a), (12b) and the last of eqs (15). Equations (12a) and (12b) are differenced using a standard five point star

$$\frac{1}{\delta x^2} (\phi_{i+1,j}^{n} - 2\phi_{ij}^{n} + \phi_{i-1,j}^{n}) + \frac{1}{\delta y^2} (\phi_{i,j+1}^{n} - 2\phi_{ij}^{n} + \phi_{i,j-1}^{n}) = D_{ij}^{n} \tag{24a}$$

$$\frac{1}{\delta x^2} (\psi_{i+1,j}^{n} - 2\psi_{ij}^{n} + \psi_{i-1,j}^{n}) + \frac{1}{\delta y^2} (\psi_{i,j+1}^{n} - 2\psi_{ij}^{n} + \psi_{i,j-1}^{n}) = - \omega_{ij}^{n} \tag{24b}$$

and the boundary conditions (13) are introduced in the usual fashion. These equations have been solved using software routines from FISHPAK [6]: eq (24a) was solved using BLKTRI and more recently using POISTG, while eq (24b) was solved using PWSCRT and more recently GENBUN. Routines BLKTRI and PWSCRT have limitations on the number of mesh points or unknowns which they can solve, whereas POISTG and GENBUN were produced more recently and are free of such limitations. Most computations were performed with the former routines, but recently several computations have been performed using the latter.

The velocities are then obtained from the potential and stream function by difference forms of eqs (11):

$$u_{ij}^{n} = \frac{1}{\delta x} (\phi_{i+1,j}^{n} - \phi_{ij}^{n}) + \frac{1}{\delta y} (\psi_{ij}^{n} - \psi_{i,j-1}^{n}) \tag{25a}$$

$$v_{ij}^{n} = \frac{1}{\delta y} (\phi_{i,j+1}^{n} - \phi_{ij}^{n}) - \frac{1}{\delta x} (\psi_{ij}^{n} - \psi_{i-1,j}^{n}) \tag{25b}$$

For the third of eqs (15), for $1 \leqslant i \leqslant I$ and $1 \leqslant j \leqslant J$,

$$\begin{aligned}
&\frac{2}{\delta x^2}\left[\frac{\tilde{p}^n_{i+1,j}-\tilde{p}^n_{ij}}{2\rho_o(j)+\tilde{\rho}^n_{i+1,j}+\tilde{\rho}^n_{ij}}-\frac{\tilde{p}^n_{ij}-\tilde{p}^n_{i-1,j}}{2\rho_o(j)+\tilde{\rho}^n_{ij}+\tilde{\rho}^n_{i-1,j}}\right]\\
&+\frac{2}{\delta y^2}\left[\frac{\tilde{p}^n_{i,j+1}-\tilde{p}^n_{ij}}{\rho_o(j+1)+\rho_o(j)+\tilde{\rho}^n_{i,j+1}+\tilde{\rho}^n_{ij}}-\frac{\tilde{p}^n_{ij}-\tilde{p}^n_{i,j-1}}{\rho_o(j)+\rho_o(j-1)+\tilde{\rho}^n_{ij}+\tilde{\rho}^n_{i,j-1}}\right]\\
&=-\frac{D^{n+1}_{ij}-D^{n-1}_{ij}}{2\delta t}+\frac{F^n_{xi-1,j}-F^n_{xij}}{\delta x}+\frac{F^n_{yi,j-1}-F^n_{yij}}{\delta y}\\
&-\frac{1}{\delta y}\left[\frac{\tilde{\rho}^n_{i,j+1}+\tilde{\rho}^n_{ij}}{\rho_o(j+1)+\rho_o(j)+\tilde{\rho}^n_{i,j+1}+\tilde{\rho}^n_{ij}}-\frac{\tilde{\rho}^n_{ij}+\tilde{\rho}^n_{i,j-1}}{\rho_o(j)+\rho_o(j-1)+\tilde{\rho}^n_{ij}+\tilde{\rho}^n_{i,j-1}}\right]
\end{aligned} \tag{26}$$

where the fluxes F^n_{xij} and F^n_{yij} are defined as follows:

for $1 \leqslant i \leqslant I-1$, $1 \leqslant j \leqslant J$

$$F^n_{xij}=\frac{1}{2\delta x}\left[(q^n_{i+1,j})^2-(q^n_{ij})^2\right]-\frac{1}{2}\left(v^n_{\omega_{ij}}\omega^n_{ij}+v^n_{\omega_{i,j-1}}\omega^n_{i,j-1}\right) \tag{27a}$$

and for $1 \leqslant j \leqslant J-1$, $1 \leqslant i \leqslant I$

$$F^n_{yij}=\frac{1}{2\delta y}\left[(q^n_{i,j+1})^2-(q^n_{ij})^2\right]+\frac{1}{2}\left(u^n_{\omega_{ij}}\omega^n_{ij}+u^n_{\omega_{i-1,j}}\omega^n_{i-1,j}\right) \tag{27b}$$

and where

$$\omega^n_{ij}=\frac{v^n_{i+1,j}-v^n_{ij}}{\delta x}-\frac{u^n_{i,j+1}-u^n_{ij}}{\delta y}$$

$$v^n_{\omega_{ij}}=\frac{1}{2}\left(v^n_{ij}+v^n_{i+1,j}\right), \qquad u^n_{\omega_{ij}}=\frac{1}{2}\left(u^n_{i,j+1}+u^n_{ij}\right)$$

$$(q^n_{ij})^2=\left(\frac{u^n_{ij}+u^n_{i-1,j}}{2}\right)^2+\left(\frac{v^n_{ij}+v^n_{i,j-1}}{2}\right)^2 \tag{27c}$$

Note that boundary conditions (7) on the normal velocities imply that $u_{0,j}=u_{I,j}=0$ for $1 \leqslant j \leqslant J$ and $v_{i,0}=v_{i,J}=0$ for $1 \leqslant i \leqslant I$. These boundary conditions are applied formally in the expressions for the fluxes $F^n_{\rho xij}$, $F^n_{\rho yij}$, F^n_{xij} and F^n_{yij} in mesh cells adjacent to boundaries. The boundary conditions (8) in discrete form become

$$\tilde{p}^n_{0,j}=\tilde{p}^n_{1,j}$$

$$\text{for } 1 \leqslant j \leqslant J \tag{28a}$$

$$\tilde{p}^n_{I,j}=\tilde{p}^n_{I+1,j}$$

$$\tilde{p}^n_{i,1} - \tilde{p}^n_{i,0} = \delta y(\tilde{\rho}^n_{i,1} + \tilde{\rho}^n_{i,0})/2$$

$$\text{for } 1 \leq i \leq I \tag{28b}$$

$$\tilde{p}^n_{i,J+1} - \tilde{p}^n_{i,J} = -\delta y(\tilde{\rho}^n_{i,J+1} + \tilde{\rho}^n_{i,J})/2$$

We note that eqs (26) together with boundary conditions (28) constitute a singular linear algebraic system of equations. When eqs (26), with boundary conditions incorporated, are summed, the left hand side sums to zero, demonstrating that all of the equations are not linearly independent. Also, the last three terms on the right hand side sum to zero, producing the requirement that the double sum over $(D^{n+1}_{ij} - D^{n-1}_{ij})/2\delta t$ must vanish. Examination of eq (30) below for D^n_{ij} shows that it has been chosen so that its double sum over all mesh points vanishes. and that the condition which must be satisfied to allow this choice produces eq (31) below for the mean pressure. Therefore, the singular linear algebraic system is seen to be consistent and thus to allow a solution. The solution is unique by noting that the double sum over all mesh points of $\tilde{p}^n_{ij}$ must be zero.

At each time step it is necessary to calculate the solution of the linear algebraic system for the pressure, eqs (26) with boundary conditions (28) incorporated. The method of solution must take into account non-uniqueness of the algebraic system. The solution method must also be able to solve large linear systems accurately, since there are IJ equations and cumulative errors from many time steps may destroy the computation. Finally, it is very important that the solution be obtained quickly since the calculation is made at each time step, and hundreds of time steps must be taken.

The solution method we have adopted is a hybrid method which combines an iterative algorithm, conjugate gradients, with a fast direct Poisson solver. The conjugate gradients algorithm provides an iterative technique for solving the linear algebraic system of equations. Details of the algorithm are presented in reference [7].

The heat source has been chosen to have the form

$$Q^n_{ij} = \hat{Q}_{ij} f^n \tag{29a}$$

$$\hat{Q}_{ij} = \left(\frac{\beta}{\pi}\right)^{1/2} \lambda \exp\left[-\beta(x_i - x_c)^2 - \lambda y_j\right] \tag{29b}$$

$$x_i = (i - 1/2)\delta x\,, \qquad y_j = (j - 1/2)\delta y \tag{29c}$$

$$f^n = Q_o \tanh At^n \tag{29d}$$

$$t^o = 0\,, \qquad t^n = \sum_{n'=0}^{n-1} \delta t^{n'} \tag{29e}$$

Hence, the discrete divergence of the velocity field becomes

$$D^n_{ij} = \frac{1}{\gamma p^n_o}\left[(\gamma - 1)\hat{Q}_{ij} - K\right] f^n \tag{30a}$$

$$K = \frac{\gamma - 1}{IJ} \sum_{i=1}^{I} \sum_{j=1}^{J} \hat{Q}_{ij} \tag{30b}$$

and the mean background pressure is found from the difference equation

$$p^{n+1}_o = p^{n-1}_o + Kf^n 2\delta t^n \tag{31}$$

with $p^0_o = p^1_o = 1$ since $f^o = 0$.

The linear stability of the algorithm is the only other consideration for discussion. A linear stability analysis of eq (18) for the density shows that the time step δt must satisfy the following condition for stability

$$\delta t^n \leq \max_{\substack{1\leq i\leq I \\ 1\leq j\leq J}} \left\{ (D_{ij}^n)^2 + \left[\frac{|U_{ij}^n|}{\delta x} + \frac{|V_{ij}^n|}{\delta y} \right]^2 \right\}^{-1/2} \tag{32}$$

where

$$U_{ij}^n \equiv (1/2)(u_{ij}^n + u_{i-1,j}^n) \tag{33a}$$

$$V_{ij}^n \equiv (1/2)(v_{ij}^n + v_{i,j-1}^n) \tag{33b}$$

When the stability condition, eq (32), is not satisfied by a time step, the time step δt^n is halved. Then the time-marching algorithm is restarted using the last time-level values as initial conditions. A first-order time step is taken and then leap-frog is resumed.

A linear stability analysis of the difference equation for the vorticity, eq (21), yields exactly the same form for the stability criterion as that found above for the density equation. Reference to figure 2b shows that the density and vorticity are evaluated at different points in the mesh, however, and therefore, the divergence D and the velocity components U and V are to be evaluated at different points than those used in eq (32). To account for the difference in the stability criterion implied above, in all calculations performed using the algorithm described above, the time step was chosen to be less than or equal to 0.8 the maximum value found for the right hand side of eq (32).

2.2.2. Lanczos Smoothing

The nonlinear nature of the equations of fluid dynamics implies that initially smooth data will, in general, produce flow fields with fine structure. Since the results presented are for finite difference computations, the resolution of the flow field is limited by the grid size used to perform the computation: structures of a size comparable to a few grid cells can be resolved, whereas smaller structures may represent artifacts of the calculations. In addition, in the computations it has been found that the calculation will eventually fail because of the intricate detail (and sharp gradients this detail represents) if the number of time steps becomes large enough.

It is for these reasons that various methods of smoothing data generated by the computations have been examined. In the method presented here, the computation is stopped periodically, with a period specified as input to the computation, and the data are smoothed spatially. The computation is restarted using the smoothed data as initial conditions, the results not being allowed to develop the intricate detail it might otherwise develop. The method used to smooth the data is a variation of one suggested by Lanczos in reference [8]. Using this method with a relatively long smoothing period, computations have been extended indefinitely.

The smoothing used here is that proposed by Lanczos, but is modified slightly for our purposes. In reference [8], the smoothed data is obtained from the value of the data at each point by adding a specified multiple of the fourth difference at that point. The change in value between the smoothed and unsmoothed data then is of order h^4 where $h \cong 1/J$ and J is the number of mesh points in one direction in space.

Since the computational scheme described here is only second order accurate in the spatial mesh size, $0(h^2)$, a less refined smoothing was used. The smoothing is accomplished by adding a specific multiple of the second-order difference at the point to the value of the datum at that point and is $0(h^2)$. When the method is generalized to two dimensions, it becomes equivalent to adding one fifth of the finite difference, five-point Laplacian to the value of the datum at each point to obtain the smoothed datum. (This is also equivalent to replacing the value at a point by the average of its value and the values of its four nearest neighbors.)

Therefore, after a specified number of time steps m, the density and vorticity data at time level m are changed according to the following prescription:

$$\rho_{ij}^m \leftarrow \rho_{ij}^m + \frac{1}{5}(\rho_{i+1,j}^m + \rho_{i-1,j}^m + \rho_{i,j+1}^m + \rho_{i,j-1}^m - 4\rho_{ij}^m) \tag{34a}$$

$$\omega_{ij}^m \leftarrow \omega_{ij}^m + \frac{1}{5}(\omega_{i+1,j}^m + \omega_{i-1,j}^m + \omega_{i,j+1}^m + \omega_{i,j-1}^m - 4\omega_{ij}^m) \tag{34b}$$

At the boundaries, the following rules are used for the smoothing. For cells adjacent to boundaries, the density is assumed to have the same value in a ficticious cell outside the boundary as its value in the cell under consideration. (This is the difference equivalent of saying that the normal derivative of the density at a boundary is zero.) The vorticity is taken to be zero on the boundary, and represents a free slip boundary condition.

A rough estimate of an equivalent Reynolds number or Grashof number introduced by smoothing can be made by the following argument. The effect of viscosity in the vorticity equation in the Boussinesq approximation arises, when the equations are made dimensionless in an appropriate way, as $\frac{1}{Re}\nabla^2\omega$, where Re is the Reynolds number, ∇^2 is the Laplacian and ω is the vorticity. The average effect per time step of Lanczos smoothing in the vorticity equation can also be represented as $\frac{ch^2}{m\delta}\nabla^2\omega$ where c is a constant of order unity, δ is the time step, h is the mesh spacing, m is the number of steps between smoothings and ∇^2 is the discretized, five-point representation of the Laplacian. Equating the coefficients of the Laplacian operators provides an estimate of the Reynolds number introduced by smoothing:

$$Re = \frac{\delta}{c}\frac{m}{h^2} = \frac{\delta}{c} mI \cdot J$$

where I and J are the number of mesh points in each direction. Taking $c = 1$, $\delta = 0.1$, $m = 40$, $I \cdot J \cong 1000$, then $Re \cong 4 \times 10^3$, and noting that the Grashof number Gr is approximately the Reynolds number squared, $Gr \cong 1.6 \times 10^7$.

3. Computational Results

As discussed in the Introduction, the vorticity, stream-function algorithm and a code implementing this algorithm were developed as a method for solving the partial differential equations derived in reference [1]. The other method for solving these equations, a finite difference method for directly integrating the equations of motion in primitive variables (density, pressure and the two components of velocity) was described in reference [2]. Reference [3] describes comparisons of the results computed using the primitive variable algorithm with analytical results obtained in special cases. These comparisons were performed to test the algorithm and the computer-code implementation. Final comparisons were made between results computed using the primitive variables code and those computed using the vorticity, stream-function code. Agreement between results was found to about five significant figures after a few time steps and to between three and four significant figures after hundreds of time steps. The discrepancy between results is smaller than the errors introduced by discretization for the mesh sizes used and well below differences which could be observed by plotting.

In this section some computational results are presented and discussed. The density, pressure and vorticity are scalar functions of the horizontal and vertical coordinates at any specified time. We have found that contours of constant value of any of these scalar quantities are a convenient way to display them. Since the temperature and density are inversely related at any particular time, contours of constant density are also contours of constant temperature.

All contour plots were prepared from a graphics package developed by the National Center for Atmospheric Research. The numbers indicating contour values are relative only. Solid lines represent values of the variable greater than zero and dashed lines represent values less than zero. For the results presented here, density and temperature are inversely related: contours of constant density have been labeled as contours of constant temperatures for illustration. Therefore, for the temperature plots, temperature contours above a reference

value appear dashed and below that reference are solid. Graphic details on the scale of a mesh cell, which is determined by the distance between fiducial marks on the sides of the plots, should be ignored.

All computations have been performed on one of three computers, the NBS UNIVAC 1108, the U.S. Treasury UNIVAC 1100/81 or the Cybernet Cyber 175. The computations require about 45K words of storage for the 31 × 31 mesh and were performed on any one of the three machines. Typical running times on the 1108, which is the machine most frequently used, is about 30 to 45 min of CPU time for 200 to 300 time steps.

In figure 3 contours of constant temperature (isotherms) are shown at four dimensionless times for a volumetric heat source centered along the floor in a square room. The rate of heat added per unit volume is largest along the floor at the center of the room and decreases in a Gaussian fashion with horizontal distance from the center and exponentially with height above the floor. The heat source is "turned-on" as a hyperbolic tangent with respect to time asymptoting to full strength around $t = 1.0$. (Note that T denotes time on the figure titles.) At the first time, $t = 2$, the problem is still linear; the flow velocities are sufficiently small than convection is unimportant, and the temperature increase in the fluid is directly proportional to the volumetric rate of heat added. Therefore, the isotherms are also contours along which the volumetric heat-addition rate is constant. (These contours are found to be parabolas.)

These computations were performed on a spatial mesh having 31 cells in the horizontal and 31 cells in the vertical directions; the tick marks along the boundary of the enclosure show the mesh cell spacing.

At time 8.5, the second frame of figure 3, a buoyant thermal has developed, giving the appearance of a mushroom cloud. The buoyant thermal intensifies in strength until the thermal hits the ceiling, as shown in the third frame, $t = 11.5$ and begins to spread. Inside the plume a distinctly periodic structure has begun to develop, as can be seen vividly in this frame; here, progressing up the plume along its centerline, one finds a local low first, then a periodic sequence of local highs and lows up to about the center of the head of the thermal.

The heated gases spread along the ceiling and fill the room from the top down, as shown in the last frame of figure 3 at $t = 14.5$. This physical behavior is exactly what is observed in room-fire tests and in other experimental observations of heating in enclosures. The symmetry about the centerline of the room displayed in these computations is some measure of the accuracy with which they were performed: the heat source is placed symmetrically, but the computations were performed as if no symmetry existed.

In figure 4 contours of constant vorticity at various times are displayed. The contours show an anti-symmetry about the centerline, as would be expected for the vorticity, and the physical features described for the density (or temperature) contours are reflected in the vorticity plots. Because the vorticity represents a higher order difference of the dependent variables, these contours display more fine scale (on the mesh scale) features than the density contours. Also, later in the computations, "noise" of a nonsymmetric and fine scale begins to show up. The vorticity plots are not as "smooth" as those of the density (or temperature).

In the first frame of figure 4 at time 2.0, early in the heating process, two vortices of equal magnitude and opposite sign develop with centers in the regions of steepest gradient of the heat source. Convection has begun by dimensionless time $t = 8.5$, frame 2 of figure 4, and the vortices are pinched together and buoyed upward off the floor. The vortices are convected toward the ceiling. Also vorticity of periodically varying strength is generated within the source region and the strength of the vorticity increases with distance above the source. Finally, frames 3 and 4 of figure 4 show that the periodically varying vorticity trains split when the ceiling is encountered and form two large regions of vorticity of opposite sign.

The pressure as a function of horizontal and vertical coordinates at any specified time can also be displayed. In figure 5 contours of constant pressure at four times during the room filling are shown. This pressure actually represents only the spatial variation of the pressure and has been normalized at each time so that its mean value is zero. This is the quantity which, together with buoyancy, induces the flow. As with the other contour plots, solid lines represent contours with values greater than zero and dashed lines indicate values less than zero. The pressure plots are seen to be smoother than those of density (temperature).

Early, the first frame at $t = 0.5$ of figure 5, the pressure is highest at the source, where heating takes place. As convection starts, the high pressure region is lifted off the floor, time $t = 2.0$: a significant enough convective velocity has developed by dimensionless time $t = 2.0$, that a low pressure region due to a Bermoulli effect can be seen at the floor. This low pressure region is associated with the high convective velocities, or the vorticity pair shown in figure 4. The low pressure region develops a double minimum, symmetric about

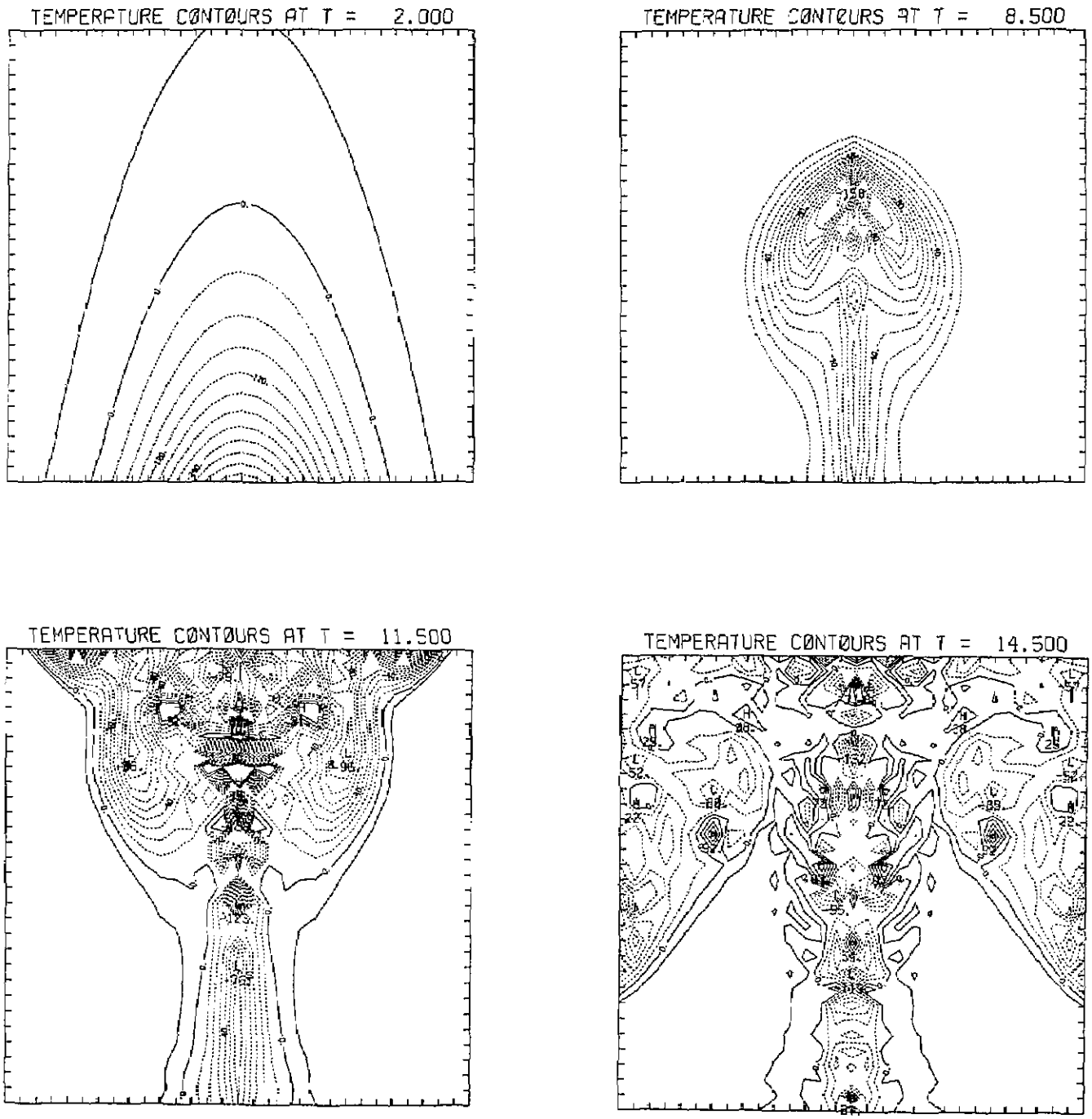

FIGURE 3. Isotherms at four dimensionless times, T, during heating by a volumetric heat source centered along the floor in a square room. These four frames illustrate (1) early heating with no convection, (2) a starting plume, (3) the plume impacting the ceiling, and (4) the room filling from the top down.

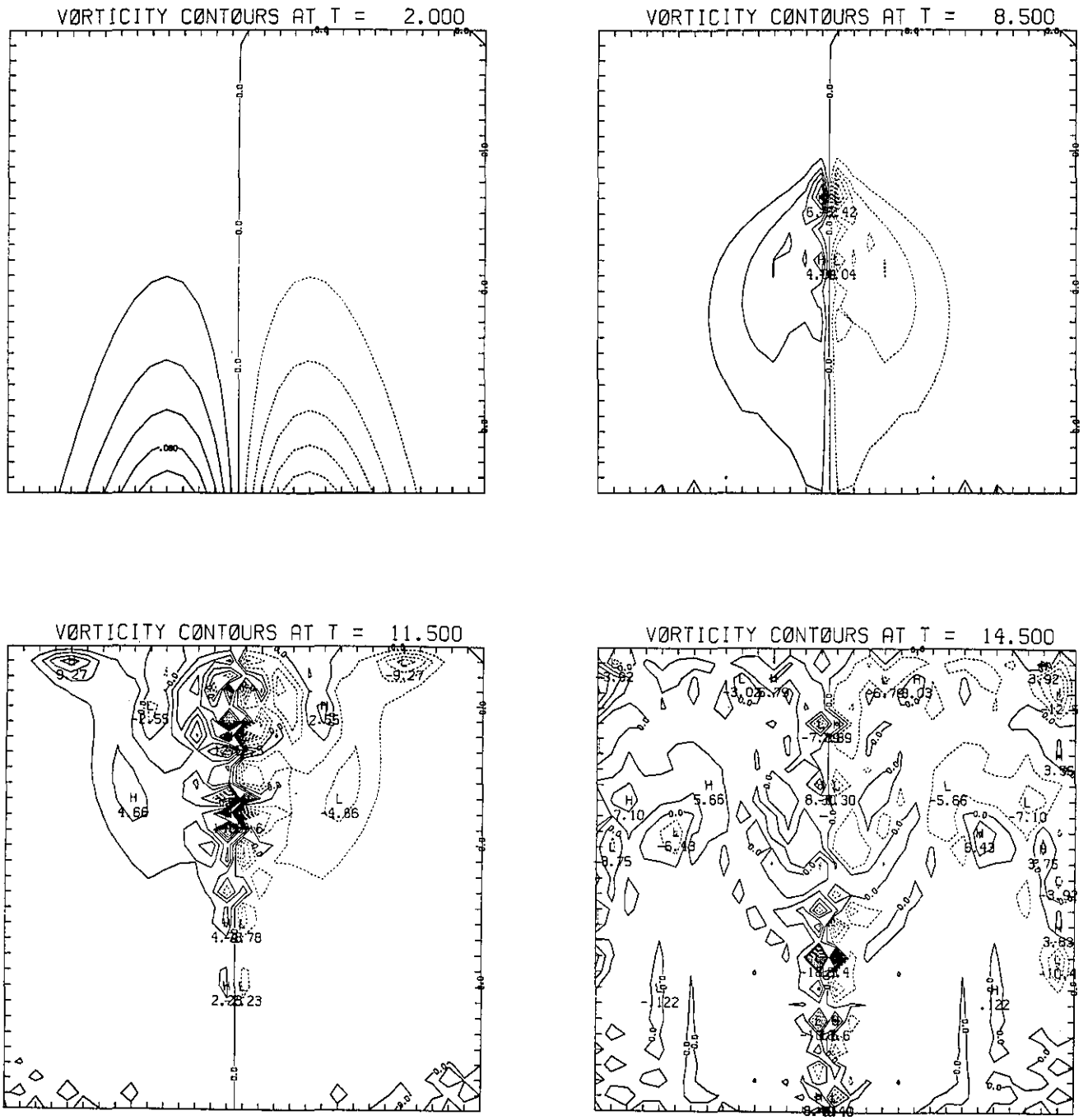

FIGURE 4. Contours of constant vorticity at four dimensionless times, T, during heating by a volumetric heat source centered along the floor in a square room. These four frames correspond to the ones shown in figure 3.

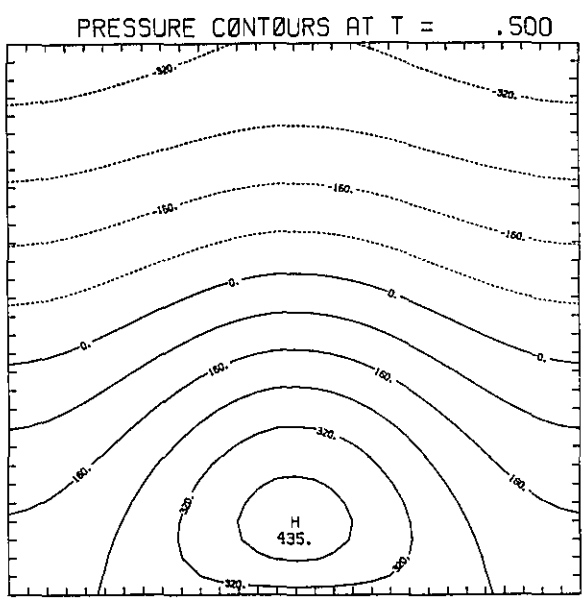

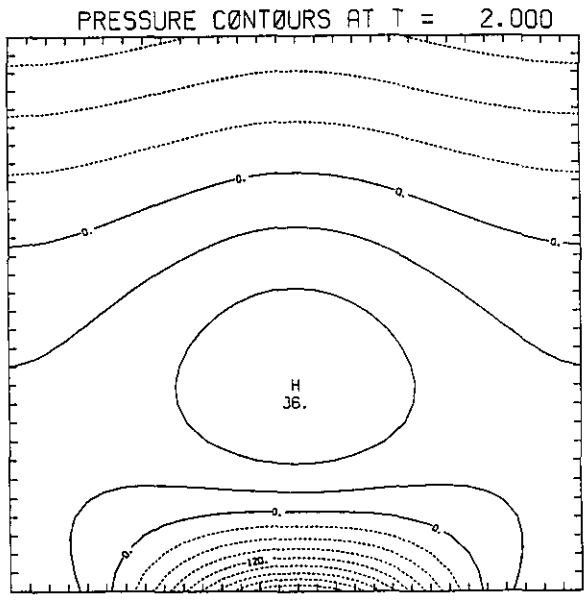

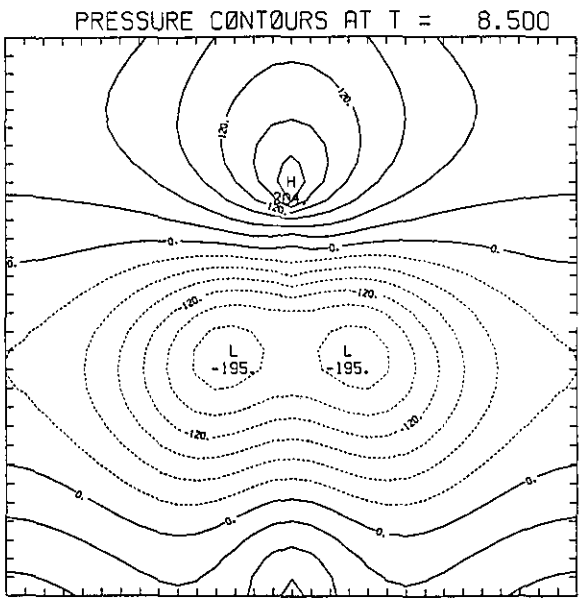

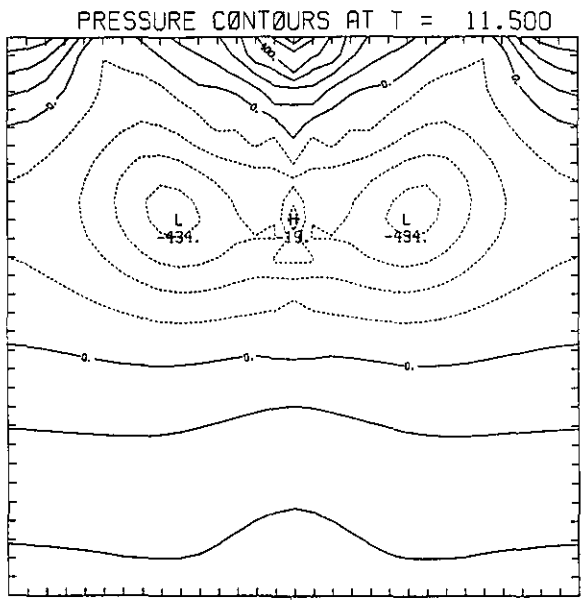

FIGURE 5. Contours of constant pressure at four dimensionless times, T, during heating. The calculation shown here is the same as that displayed in figures 3 and 4, but the times are chosen to illustrate the stages in the development of the pressure field.

the room centerline as seen at time 8.5 and rises to the ceiling, as shown in figure 5, time 11.5, where a strong compression develops at the center of the ceiling. The final pressure diagram displays the double minimum, associated with the strong vortex pair and high temperature shown in figures 3 and 4, separating and moving toward the walls.

In figures 6 and 7 contours of constant potential ϕ and constant stream function ψ are shown. Only one plot of the potential is shown because the spatial dependence does not change with time: the potential function is separable in space and time. Four frames of stream function are shown in figure 7. The stream function is antisymmetrical about the centerline and displays a peak and a valley which slowly rise toward the ceiling. The stream function is rather smooth, showing only a slightly wavy behavior at later times.

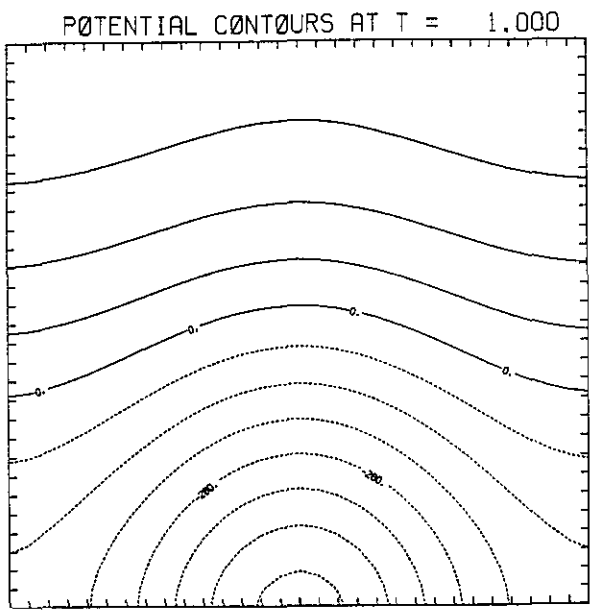

FIGURE 6. Velocity-potential contours at dimensionless time, $T = 1.0$ for the calculation displayed in figures 3–5. The potential function is a function of space times a function of time; therefore, the spatial dependence does not change with time.

The base computation, shown in figures 3–7, was repeated several times with smoothing introduced at different numbers of time steps. Figures 8 and 9 compare constant temperature contours at dimensionless time 11.5 and 14.5 respectively determined by the base computation, on the upper left, and by three levels of smoothing in the other three plots of each figure. It is seen that the fine structure is eliminated by smoothing, but large scale features are still retained. In figure 8 four plots of constant temperature contours at approximately the same time are compared. The plot in the upper left hand corner is the unsmoothed computation. The plot at the upper right is the result of the computation smoothed only once up until that time, after $N = 160$ time steps. The next plot, lower left, is from a computation smoothed every 80 time steps, that in the lower right is from a computation smoothed every 40 time steps. Figure 9 shows a similar comparison of the effects of smoothing, but at approximately $t = 14.5$. These plots show clearly the loss in detail with increasing frequency of smoothing or increased simulated viscosity. They also show that the buoyant plume rise slows due to the decreasing gradients. The smoothing and loss of fine-scale detail with increased frequency of smoothing are apparent, and, in fact, these results appear much closer qualitatively to results obtained in previous studies which integrated the Navier-Stokes equations by finite difference techniques (for example, reference [9], figures 4 and 5).

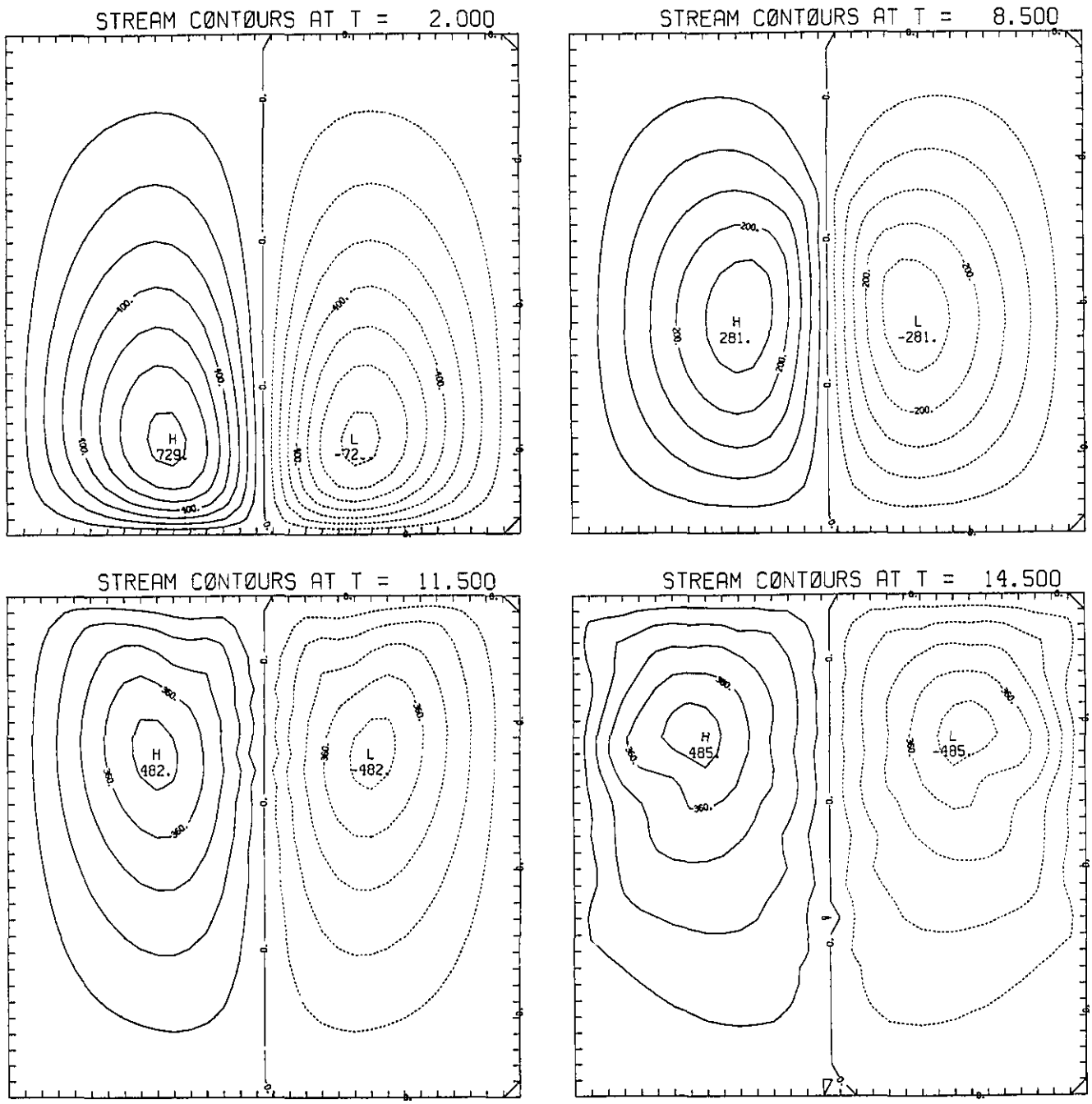

FIGURE 7. *Stream-function contours at four dimensionless times corresponding to the times displayed in figures 3 and 4.*

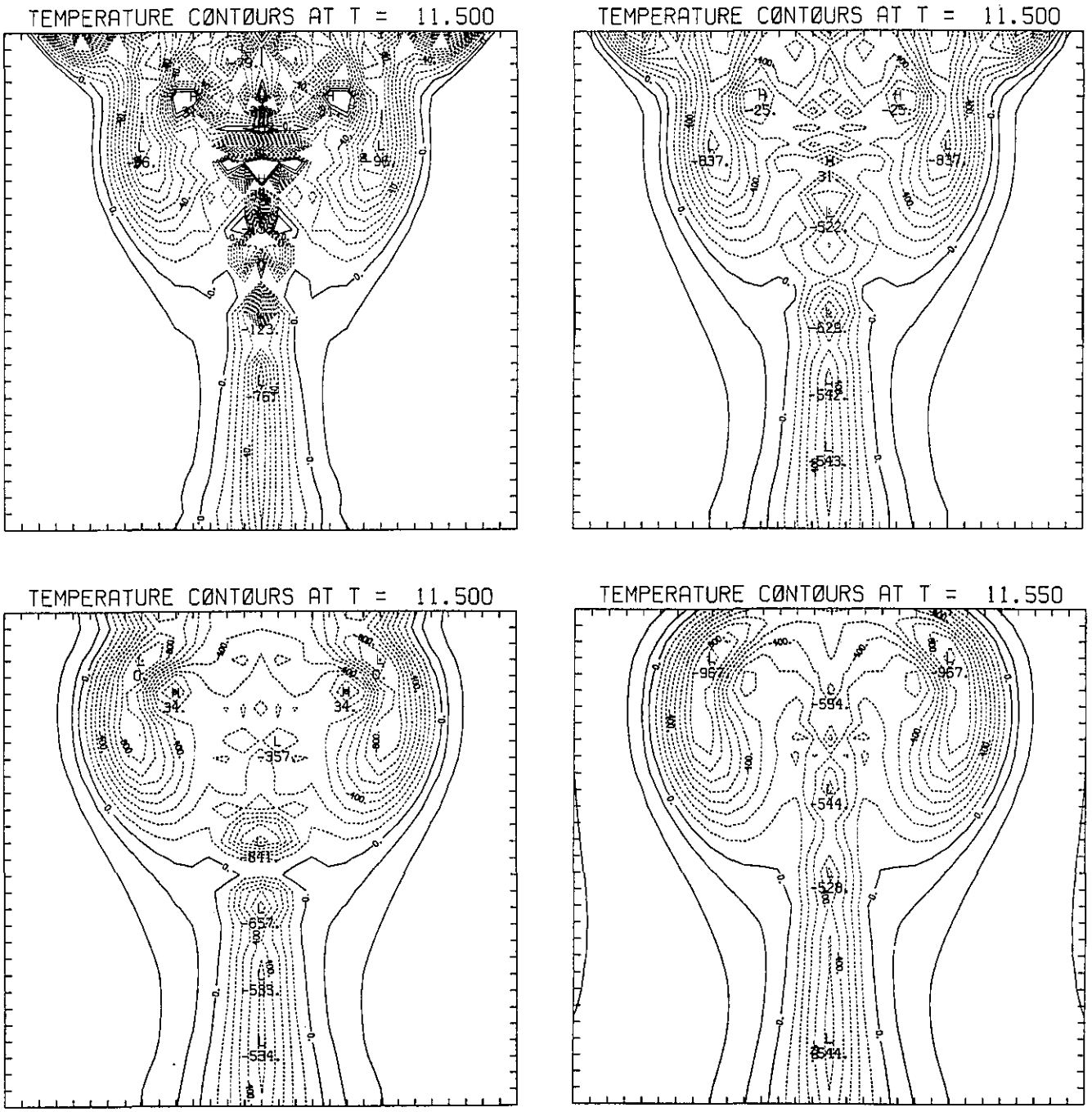

FIGURE 8. Isotherms at approximately the same dimensionless time, T, with Lanczos smoothing applied at different frequencies. The frame in the upper left corner is the unsmoothed computation. The frame at the upper right is smoothed every 160 time steps, that at the lower left every 80 time steps and that at the lower right every 40 time steps.

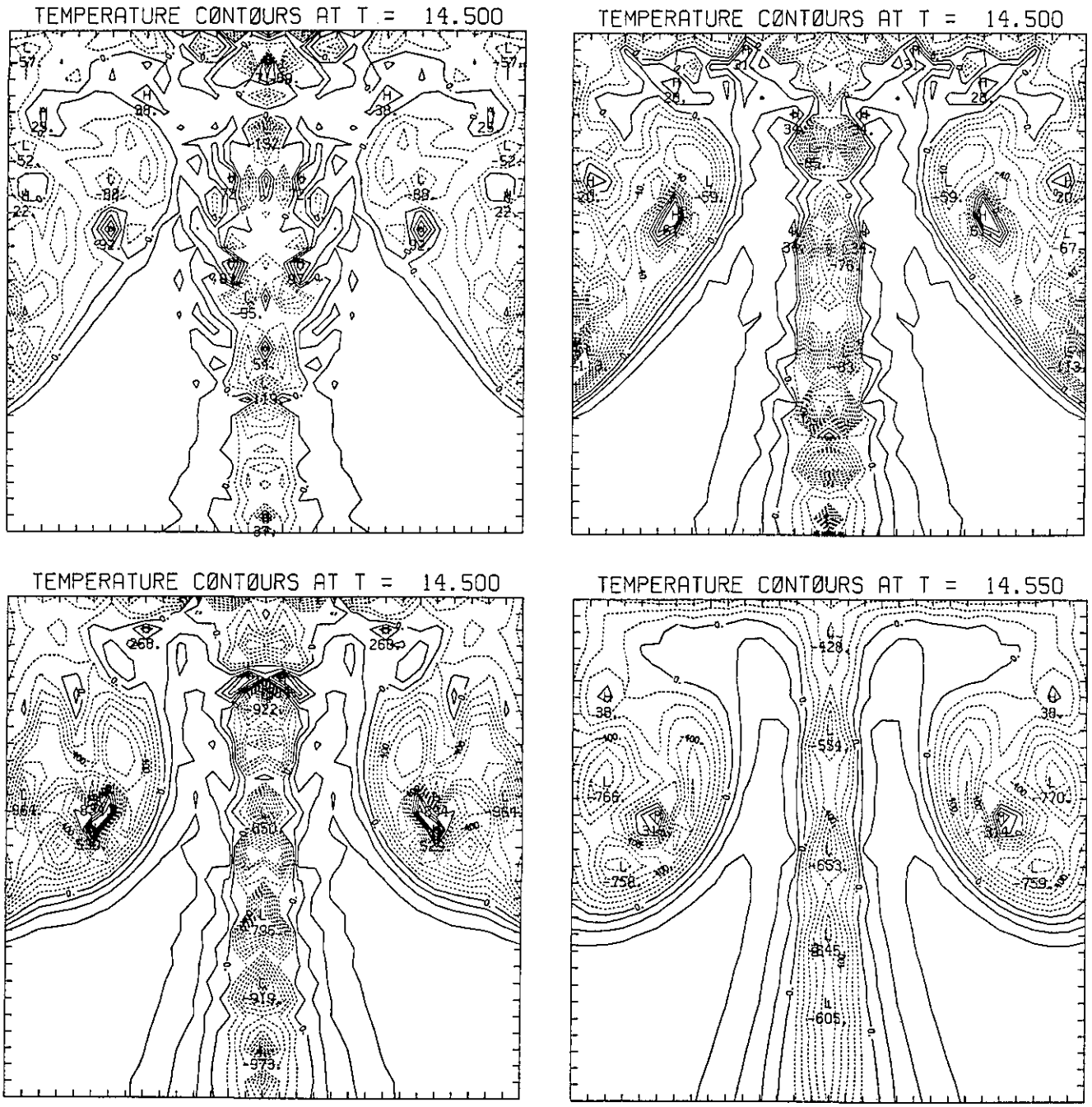

FIGURE 9. Isotherms at approximately the same dimensionless time, T, with Lanczos smoothing applied at different frequencies. The frame in the upper left corner is the unsmoothed computation. The frame in the upper right is smoothed every 160 time steps, that at the lower left every 80 time steps and that at the lower right every 40 time steps.

4. References

[1] Rehm, R. G. and Baum, H. R., The Equations of Motion for Thermally Driven Buoyant Flows, J. Res. Nat. Bur. Standards **83**, No. 3, pp. 297–308 (May-June 1978).

[2] Baum, H. R., Rehm, R. G., Barnett, P. D., and Corley, D. M., Finite Difference Calculations of Buoyant Convection in an Enclosure, Part I: Basic Algorithm, Nat. Bur. Stand. (U.S.) NBSIR 81–2385 (Dec. 1981).

[3] Rehm, R. G., Baum, H. R., Barnett, P. D. and Corley, D. M., Finite Difference Calculations of Buoyant Convection in an Enclosure, Part II: Verification of the Basic Algorithm, National Bureau of Standards Technical Note in preparation.

[4] Baum, H. R. and Rehm, R. G., Finite Difference Solutions for Internal Waves in an Enclosure, National Bureau of Standards Report in preparation.

[5] Harlow, F. H. and Amsden, A. A., *Fluid Dynamics, A LASL Monograph*, Los Alamos Scientific Laboratory Report LA4700, Los Alamos, New Mexico (June 1971).

[6] Swarztrauber, P. and Sweet, R., Efficient FORTRAN Subprograms for the Solution of Elliptic Partial Differential Equations, NCAR-TN/IA-109 (July 1975).

[7] Lewis, J. G. and Rehm, R. G., The Numerical Solution of a Nonseparable Elliptic Partial Differential Equation by Preconditioned Conjugate Gradients, J. Res. Nat. Bur. Standards **85**, No. 5, pp. 367–390 (Sept.–Oct. 1980).

[8] Lanczos, C., *Applied Analysis*, Prentice Hall, Inc., Englewood Cliffs, New Jersey, 1956, pp. 316–320.

[9] Knight, C., Numerical Studies of Natural Convection in an Enclosure, Harvard University Division of Engineering and Applied Physics, Technical Report No. 15.

[10] Kreiss, H. and Oliger, J., Methods for the Approximate Solution of Time Dependent Problems, Global Atmospheric Research Programme (GARP) Publication Series No. 10, February 1973.